EUROPEAN ORGANIZATION FOR NUCLEAR RESEARCH

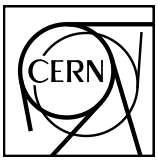


CERN-EP-2026-206
July 18, 2026

# First Observation of an Exotic Reggeon

The COMPASS Collaboration

**Abstract**

We present new COMPASS high-statistics measurements of the peripheral production of $\eta\pi^-$ and $\eta'\pi^-$ pairs in the reactions $\pi^- p \to \eta^{(\prime)}\pi^- p$. For the first time, we perform an unbinned analysis of the high-mass region of the $\eta\pi^-$ and $\eta'\pi^-$ systems, which allows us to disentangle the exchange mechanisms governing their production. We report the first observation in high-energy scattering of an exotic Reggeon with high significance exceeding $5\,\sigma$ for both channels, which is, most likely, related to the exotic $\pi_1(1600)$.

*(to be submitted to PRL)*

CERN-EP-2026–209, JLAB-THY-26-4814, MIT-CTP/6061

# First Observation of an Exotic Reggeon

G. D. Alexeev,[1] M. G. Alexeev,[2,3] C. Alice,[2,3] A. Amoroso,[2,3] V. Andrieux,[4] V. Anosov,[1] K. Augsten,[5] W. Augustyniak,[6] C. D. R. Azevedo,[7] B. Badelek,[8] R. Beck,[9] J. Beckers,[10] Y. Bedfer,[11] V. Benešová,[12] J. Bernhard,[13] F. Bradamante,[14] A. Bressan,[15,14,a] W.-C. Chang,[16] C. Chatterjee,[14,b] M. Chiosso,[2,3] S.-U. Chung,[10,c] A. Cicuttin,[14,17] M. L. Crespo,[14,17] D. D'Ago,[15,14] S. Dalla Torre,[14] S. S. Dasgupta,[18,d] S. Dasgupta,[14,e] M. Dehpour,[12] F. Delcarro,[2,3] I. Denisenko,[1] O. Yu. Denisov,[3] S. V. Donskov,[19,20] N. Doshita,[21] Ch. Dreisbach,[10] W. Dünnweber,[f] R. R. Dusaev,[19,20] D. Ecker,[10] P. Faccioli,[22] M. Faessler,[f] M. Finger,[12,d] M. Finger jr.,[12] H. Fischer,[23] K. J. Flöthner,[9] W. Florian,[14,17] J. M. Friedrich,[10] V. Frolov,[1] L.G. Garcia Ordòñez,[14,17] O. P. Gavrichtchouk,[1] S. Gerassimov,[20,10] J. Giarra,[24] D. Giordano,[2,3,g] A. Grasso,[2,3] A. Gridin,[1] M. Grosse Perdekamp,[4] B. Grube,[10] M. Grüner,[9] A. Guskov,[1] P. Haas,[10] D. von Harrach,[24] M. Hoffmann,[9,b] N. d'Hose,[11,b] C.-Y. Hsieh,[16] S. Ishimoto,[21,h] A. Ivanov,[1] T. Iwata,[21] V. Jary,[5] R. Joosten,[9] E. Kabuß,[24,b] F. Kaspar,[10] A. Kerbizi,[15,14] B. Ketzer,[9] G. V. Khaustov,[20] J. H. Koivuniemi,[25,4] V. N. Kolosov,[19,20] K. Kondo Horikawa,[21] I. Konorov,[20,10] A. Yu. Korzenev,[1] A. M. Kotzinian,[19] O. M. Kouznetsov,[1] A. Koval,[6] F. Kunne,[11] K. Kurek,[6] R. P. Kurjata,[26] G. Kurten,[10,i] A. Květoň,[12] K. Lavickova,[5] S. Levorato,[14] Y.-S. Lian,[16,j] J. Lichtenstadt,[27] P.-J. Lin,[28,b] R. Longo,[4] V. E. Lyubovitskij,[20,k] A. Maggiora,[3] N. Makke,[14] G. K. Mallot,[13,23] A. Maltsev,[1] A. Martin,[15,14] J. Marzec,[26] J. Matoušek,[12] T. Matsuda,[29] C. Menezes Pires,[22] F. Metzger,[9] W. Meyer,[25] E. Mitrofanov,[1] D. Miura,[21] Y. Miyachi,[21] R. Molina,[14,17] A. Moretti,[15,14] D. Neyret,[11] M. Niemiec,[8] J. Nový,[5] W.-D. Nowak,[24] G. Nukazuka,[21,l] A. G. Olshevsky,[1] M. Ostrick,[24] D. Panzieri,[3,m] B. Parsamyan,[19,3,13] S. Paul,[10] H. Pekeler,[9,n] J.-C. Peng,[4] M. Pešek,[12] D. V. Peshekhonov,[1] M. Pešková,[12] S. Platchkov,[11] J. Pochodzalla,[24] V. A. Polyakov,[1,20] P. Pucci,[12] C. Quintans,[22,6] G. Reicherz,[25] C. Riedl,[4] D. I. Ryabchikov,[20,10] A. Rychter,[26] V. D. Samoylenko,[19,20] A. Sandacz,[6,b] S. Sarkar,[18] I. A. Savin,[1,d] G. Sbrizzai,[14] H. Schmieden,[30] A. Selyunin,[1] S. Seriubin,[1] L. Sinha,[18] D. Spülbeck,[9] A. Srnka,[31] M. Stolarski,[6,a] M. Sulc,[32] H. Suzuki,[21,o] S. Tessaro,[14] F. Tessarotto,[14] A. Thiel,[9] F. Tosello,[3] A. Townsend,[4,p] V. Tskhay,[20] B. Valinoti,[14,17] B. M. Veit,[24] J.F.C.A. Veloso,[7] A. Vijayakumar,[4] M. Virius,[5] M. Wagner,[9] S. Wallner,[10,i] K. Zaremba,[26] M. Zavertyaev,[20] M. Zemko,[5] E. Zemlyanichkina,[1] and M. Ziembicki[26]

(COMPASS Collaboration)

C. Fernández-Ramírez,[33,q] M. Mikhasenko,[34,r] Ł. Bibrzycki,[35] G. Foti,[36,37] N. Hammoud,[38] V. Mathieu,[38] G. Montaña,[38] R. J. Perry,[39] A. Pilloni,[36,37] A. Rodas,[40,41] V. Shastry,[42,43] W. A. Smith,[36,44,45,46] A. P. Szczepaniak,[41,42,43] and D. Winney[47]

(Joint Physics Analysis Center)

[1] *Affiliated with an international laboratory covered by a cooperation agreement with CERN*
[2] *University of Torino, Dept. of Physics, 10125 Torino, Italy*
[3] *Torino Section of INFN, 10125 Torino, Italy*
[4] *University of Illinois at Urbana-Champaign, Dept. of Physics, Urbana, IL 61801-3080, USA*
[5] *Czech Technical University in Prague, 16636 Prague, Czech Republic*
[6] *National Centre for Nuclear Research, 02-093 Warsaw, Poland*
[7] *University of Aveiro, I3N, Dept. of Physics, 3810-193 Aveiro, Portugal*
[8] *University of Warsaw, Faculty of Physics, 02-093 Warsaw, Poland*
[9] *Universität Bonn, Helmholtz-Institut für Strahlen- und Kernphysik, 53115 Bonn, Germany*
[10] *Technische Universität München, Physik Dept., 85748 Garching, Germany*
[11] *IRFU, CEA, Université Paris-Saclay, 91191 Gif-sur-Yvette, France*
[12] *Charles University, Faculty of Mathematics and Physics, 12116 Prague, Czech Republic*
[13] *CERN, 1211 Geneva 23, Switzerland*
[14] *Trieste Section of INFN, 34127 Trieste, Italy*
[15] *University of Trieste, Dept. of Physics, 34127 Trieste, Italy*
[16] *Academia Sinica, Institute of Physics, Taipei 11529, Taiwan*
[17] *Abdus Salam ICTP, 34151 Trieste, Italy*
[18] *Matrivani Institute of Experimental Research & Education, Calcutta-700 030, India*
[19] *A.I. Alikhanyan National Science Laboratory, 2 Alikhanyan Br. Street, 0036, Yerevan, Armenia*
[20] *Affiliated with an institute formerly covered by a cooperation agreement with CERN*

[21] Yamagata University, Yamagata 990-8560, Japan
[22] LIP, 1649-003 Lisbon, Portugal
[23] Universität Freiburg, Physikalisches Institut, 79104 Freiburg, Germany
[24] Universität Mainz, Institut für Kernphysik, 55099 Mainz, Germany
[25] Universität Bochum, Institut für Experimentalphysik, 44780 Bochum, Germany
[26] Warsaw University of Technology, Institute of Radioelectronics, 00-665 Warsaw, Poland
[27] Tel Aviv University, School of Physics and Astronomy, 69978 Tel Aviv, Israel
[28] Center for High Energy and High Field Physics and Dept. of Physics, National Central University, 300 Zhongda Rd., Zhongli 320317, Taiwan
[29] University of Miyazaki, Miyazaki 889-2192, Japan
[30] Universität Bonn, Physikalisches Institut, 53115 Bonn, Germany
[31] Institute of Scientific Instruments of the CAS, 61264 Brno, Czech Republic
[32] Technical University in Liberec, 46117 Liberec, Czech Republic
[33] Departamento de Física Interdisciplinar, Universidad Nacional de Educación a Distancia (UNED), Madrid E-28040, Spain
[34] Fakultät für Physik und Astronomie, Ruhr-Universität Bochum, Bochum D-44780, Germany
[35] AGH University of Krakow, Faculty of Physics and Applied Computer Science, Kraków PL-30-059, Poland
[36] Dipartimento di Scienze Matematiche e Informatiche, Scienze Fisiche e Scienze della Terra, Università degli Studi di Messina, Messina I-98166, Italy
[37] INFN Sezione di Catania, Catania I-95123, Italy
[38] Departament de Física Quàntica i Astrofísica and Institut de Ciències del Cosmos, Universitat de Barcelona, Barcelona E-08028, Spain
[39] Center for Theoretical Physics, Massachusetts Institute of Technology, Cambridge, Massachusetts 02139, USA
[40] Department of Physics, Old Dominion University, Norfolk, Virginia 23529, USA
[41] Theory Center, Thomas Jefferson National Accelerator Facility, Newport News, Virginia 23606, USA
[42] Center for Exploration of Energy and Matter, Indiana University, Bloomington, Indiana 47403, USA
[43] Department of Physics, Indiana University, Bloomington, Indiana 47405, USA
[44] Nuclear Science Division, Lawrence Berkeley National Laboratory, Berkeley, California 94720, USA
[45] Department of Physics, University of California, Berkeley, California 94720, USA
[46] Department of Physics, William & Mary, Williamsburg, Virginia 23187, USA
[47] Instituto de Ciencias Nucleares, Universidad Nacional Autónoma de México, Ciudad de México 04510, Mexico

We present new COMPASS high-statistics measurements of the peripheral production of $\eta\pi^-$ and $\eta'\pi^-$ pairs in the reactions $\pi^- p \to \eta^{(\prime)}\pi^- p$. For the first time, we perform an unbinned analysis of the high-mass region of the $\eta\pi^-$ and $\eta'\pi^-$ systems, which allows us to disentangle the exchange mechanisms governing their production. We report the first observation in high-energy scattering of an exotic Reggeon with high significance exceeding $5\,\sigma$ for both channels, which is, most likely, related to the exotic $\pi_1(1600)$.

*Introduction.*— Understanding the hadron spectrum in terms of quark and gluon degrees of freedom of quantum chromodynamics (QCD) is a central goal of nonperturbative strong-interaction physics [1, 2]. Many exotic states beyond the naïve quark model [3] have now been identified, predominantly with heavy quarks [4–8] but also with light ones [9]. Candidates for some of the latter are *hybrid mesons* [10–16], *i.e.* hadrons with an explicit gluonic excitation that provides a direct probe of low-energy gluon dynamics [17–19]. Hybrids are resonances and, therefore, are identified through the final states they decay into. In particular, final states of $\eta\pi$ and $\eta'\pi$ with odd angular momentum are relevant because they explicitly carry exotic quantum numbers that cannot be obtained with a quark-antiquark pair. These final states have long served as benchmark channels in the search for hybrid mesons. Early evidence came from two mass regions: a structure near 1.4 GeV/$c^2$ in $\eta\pi^-$, observed by E852 at BNL [20, 21] and Crystal Barrel at CERN [22], and a heavier one near 1.6 GeV/$c^2$ in $\eta'\pi^-$, reported by VES [23] and E852 [24]. High-statistics measurements by COMPASS [25, 26] later established both peaks unambiguously. The puzzle of whether they correspond to one state or two was resolved by a JPAC coupled-channel analysis of the COMPASS data [27]. The analysis showed that a single spin-exotic resonance, the $\pi_1(1600)$, accounts for both structures. This identification matches theoretical expectations for the lightest hybrid meson [28–33] and has since been reinforced by independent coupled-channel analyses [34, 35] and lattice QCD calculations [36].

High-energy reactions can be parametrized in terms of exchanges of towers of increasing-spin states known collectively as Reggeons. All particles in a Reggeon are identified by a trajectory $J = \alpha(p^2)$ that relates the spin $J$ of each particle to its invariant mass squared $p^2$, as long as $p^2 > 0$. In the spacelike region $p^2 < 0$ is the momentum transferred in the reaction. In that case, the trajectory collectively determines the energy dependence of the cross section. Conventionally, the Reggeon takes the name of the lightest particle lying on the trajectory [37, 38]. In the reactions under study, $\pi^- p \to \eta^{(\prime)}\pi^- p$, the discrete quantum numbers of external particles are such that odd spin exchanges are mani-

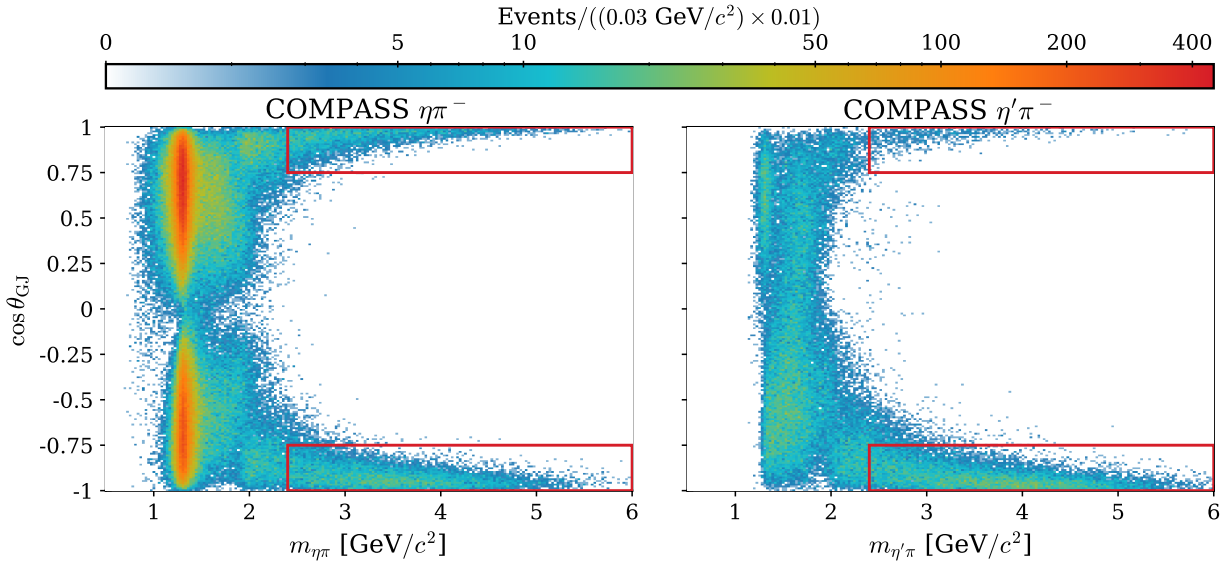


FIG. 1. $\eta\pi^-$ (left) and $\eta'\pi^-$ (right) event distributions in logarithmic scale, integrated over the four-momentum transfer to the target proton in the range $t_p \in [-1, -0.1]$ GeV$^2/c^2$ and azimuthal angle. The red boxes mark the region fitted in this analysis. The fast-$\eta^{(\prime)}$ region corresponds to $\cos\theta_{\mathrm{GJ}} > 0$. The forward-backward asymmetry $A(m_{\eta\pi})$ is obtained as the difference between the forward and backward events for a given $m_{\eta\pi}$ bin, divided by the sum.

festly exotic. The difference between odd and even spin exchanges is reflected in the dependence of the cross sections on the kinematic variables, and therefore can be determined from data.

In this Letter, we report the first observation of an exotic Reggeon, with significances of $9.9\,\sigma$ in $\eta\pi^-$ and $5.5\,\sigma$ in $\eta'\pi^-$, most plausibly identified with the exchange of the exotic $\pi_1(1600)$. This was achieved using an event-based analysis of recent COMPASS measurements of peripheral $\eta^{(\prime)}\pi^-$ production in the double-Regge (DR) regime that allowed us to disentangle the dominant exchanges, and identify the presence of an exotic trajectory.

*COMPASS data.*— The COMPASS experiment is a forward spectrometer located at CERN SPS [39]. The setup used for collecting data of this analysis is described in Ref. [40]. COMPASS collected data for two years with a negatively charged hadron beam (97% $\pi^-$) on a proton target. We analyze the complete $\eta^{(\prime)}\pi^-$ data set, which extends up to $m_{\eta\pi} = 6\,\mathrm{GeV}/c^2$; throughout this Letter, the $\eta$ subscript denotes both $\eta$ and $\eta'$ in kinematic variables. To isolate the production of the $\eta\pi$ system, we require three charged tracks from the primary vertex and exactly two photon clusters. Fiducial cuts on energy and kinematics are applied to select exclusive reactions. For $\eta\pi^-$ ($\eta'\pi^-$), we reconstruct $\pi^0$ ($\eta$) via a kinematic fit within a tight window in the diphoton invariant mass, then cut on $\pi^+\pi^-\gamma\gamma$ invariant mass to match the $\eta$ ($\eta'$). The resulting samples contain $\sim$ 270,000 ($\sim$ 85,000) events from threshold up to $6\,\mathrm{GeV}/c^2$ with four-momentum transfer to the target proton in the range $t_p \in [-1, -0.1]$ GeV$^2/c^2$; further details are given in Ref. [41].

Figure 1 shows $m_{\eta\pi}$ versus $\cos\theta_{\mathrm{GJ}}$, the cosine of the angle between the $\eta^{(\prime)}$ and the beam in the Gottfried-Jackson frame [41–43]. The details on the kinematic variables can be found in the End Matter. Above $2\,\mathrm{GeV}/c^2$, the distributions peak sharply in the forward and backward regions, where the $\eta^{(\prime)}$ or the $\pi$ carries most of the beam momentum; these are named the fast-$\eta$ and fast-$\pi$ regions, respectively. The peaks narrow with increasing $m_{\eta\pi}$, characteristic of diffractive processes for which DR exchange is the expected dominant mechanism [43–45].

*Production amplitude.*— A $2 \to 3$ process is kinematically described by three energy variables ($s$, $s_{12}$, $s_{2p}$) and two momentum transfers ($t_1$, $t_p$). When all energies are large and momentum transfers small, the reaction is dominated by the exchange of a top Reggeon $\mathbb{R}_t$ between the produced mesons and a bottom Reggeon $\mathbb{R}_b$ between the proton and the meson shown in the middle of **??**—the DR mechanism [37, 43–46]. Previous COMPASS analyses were performed in the single Regge kinematics where the meson system is produced in the resonance region. At small momentum transfer, the Regge trajectories are approximately linear and only a few Reggeons are expected to contribute. Reggeons with the largest trajectory are referred to as leading. Quantum numbers of external particles restrict the possible exchanges. For diffractive processes, the bottom exchange is dominantly Pomeron ($\mathbb{P}$), with possible subleading corrections due to the $f_2$. For the top exchange, quantum numbers of

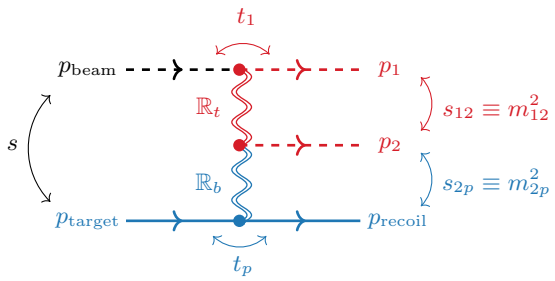


FIG. 2. Diagrammatic representation of the DR production mechanism. The meson produced with small momentum transfer $t_1$ from the beam carries the largest momentum and is referred to as fast. Fast-$\eta$ (fast-$\pi$) amplitudes correspond to final states $1 = \eta^{(\prime)}$ ($\pi$) and $2 = \pi$ ($\eta^{(\prime)}$). The exchanged Reggeons are $\mathbb{R}_t = a_2$, $a_2'$, or $\pi_1$ ($f_2$ or $\mathbb{P}$) at the top vertex and $\mathbb{R}_b = f_2$ or $\mathbb{P}$ at the bottom vertex. Six amplitudes, $\mathbb{R}_t\mathbb{R}_b = a_2 f_2$, $a_2\mathbb{P}$, $a_2' f_2$, $a_2'\mathbb{P}$, $\pi_1 f_2$, and $\pi_1\mathbb{P}$, can contribute to the forward region, while four, $\mathbb{R}_t\mathbb{R}_b = f_2 f_2$, $f_2\mathbb{P}$, $\mathbb{P}f_2$, and $\mathbb{P}\mathbb{P}$, can contribute to the backward region.

beam and produced particles will force natural parity, and $I^G = 1^-$ ($I^G = 0^+$) for the fast-$\eta$ (fast-$\pi$) amplitude, with isospin $I$ and $G$-parity $G$. This implies that the possible top exchanges for fast-$\pi$ are the even-spin $\mathbb{P}$ or $f_2$, with odd-spins forbidden by Bose symmetry. For fast-$\eta$, the leading exchange is expected to be the ordinary $a_2$, but as subleading Reggeons both the even-spin (ordinary) $a_2'$ and the odd-spin (exotic) $\pi_1$ are allowed. We construct our reaction model adopting the framework of Refs. [43, 45, 47, 48], with the addition of form factors. The explicit expressions are given in the End Matter.

*Event fitting.*— Acceptance effects are accounted for using Monte Carlo samples for the $\eta^{(\prime)}\pi^-$ final state propagated through the COMPASS simulation framework `TGEANT` [49], based on `GEANT4` [50], and reconstructed and selected as for real data. The model parameters are extracted from an unbinned event-by-event fit to the data using the extended negative log-likelihood (ENLL) method [9]. The fit and the uncertainties are computed using `ROOT`'s `TMinuit2` package [51]. The two channels are fitted independently; further details are given in the End Matter. Our event-by-event analysis is sensitive to angular correlations and this allows us to resolve the momentum-transfer dependence.

We select the data in the range of validity of the model: forward and backward regions, $|\cos\theta_{\text{GJ}}| > 0.75$, and high-energies interval $2.4 < m_{\eta\pi} \lesssim 6\,\text{GeV}/c^2$, that is safely above the resonance region, also used in Ref. [43]. These regions are marked by the red boxes in Fig. 1 and contain 23,727 (21,421) events in the $\eta\pi^-$ ($\eta'\pi^-$) channel.

*Results.*— First, we fit with only the DR amplitudes of the base model made of only the six leading ordinary exchange amplitudes $A_i$ labeled by their top and bottom

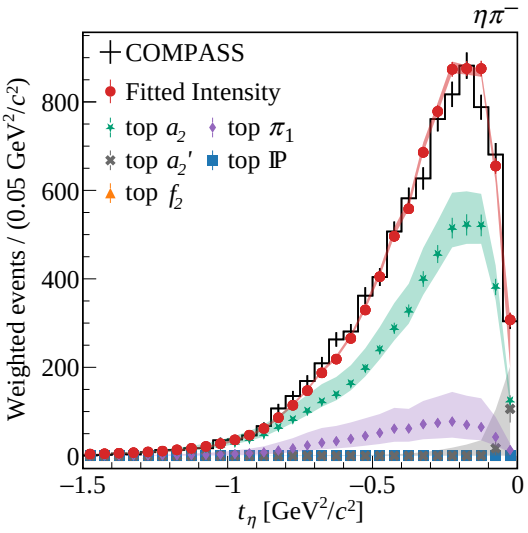


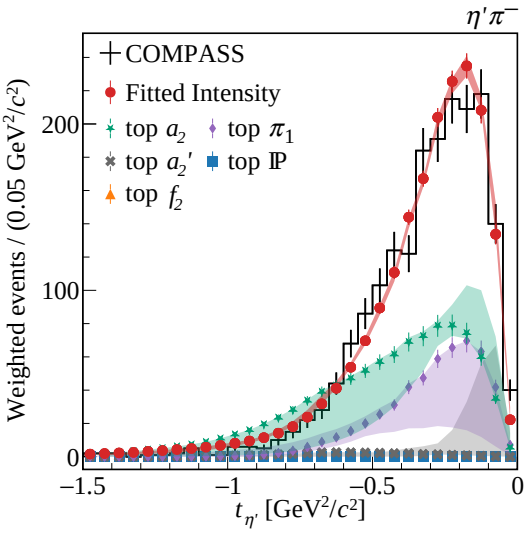


FIG. 3. Weighted intensity distributions at small $t_\eta$ for the individual top-exchange contributions in the $\eta\pi^-$ (top) and $\eta'\pi^-$ (bottom) channels. Small $t_\eta$ corresponds $\cos\theta_{\text{GJ}} \sim 1$. By top $\pi_1$, $a_2$, $f_2$ and $\mathbb{P}$ we refer to the coherent sum of the amplitudes whose exchanged $\mathbb{R}_t$ is the $\pi_1$, $a_2$, $f_2$ and $\mathbb{P}$, respectively. Note that the top $f_2$ and $\mathbb{P}$ exchanges are negligible, as expected. Systematic uncertainties are provided as a band. Data and fit include the acceptance of the COMPASS apparatus.

Reggeons, namely $a_2 f_2$, $a_2\mathbb{P}$, $f_2 f_2$, $f_2\mathbb{P}$, $\mathbb{P}f_2$, and $\mathbb{P}\mathbb{P}$. The model fails to describe the binned intensity distributions as shown in the Supplemental Material [52]. A reasonable description of the data would require raising the lower bound to $m_{\eta\pi} = 4$ GeV/$c^2$, which is much higher than the typical onset of the DR region. The discrepancy originates from forward-peak events, indicating that ad-

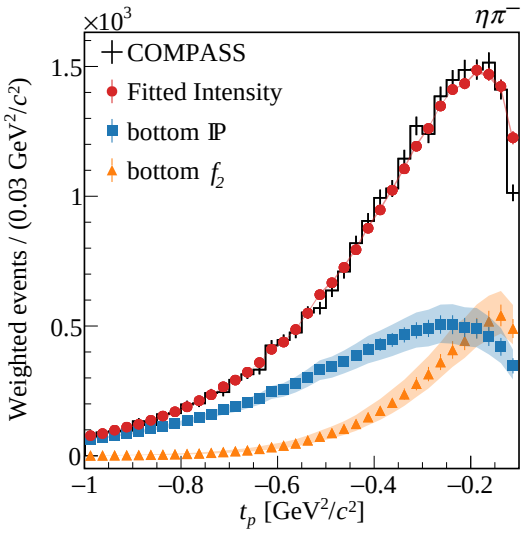


FIG. 4. Weighted intensity distributions at small $t_p$ for the individual bottom-exchange contributions in the $\eta\pi^-$ channel. Results are similar for the $\eta'\pi^-$ channel. By bottom $\mathbb{P}$ (bottom $f_2$) we refer to the coherent sum of the amplitudes whose exchanged $\mathbb{R}_b$ is the $\mathbb{P}$ ($f_2$). Systematic uncertainties are provided as a band. Data and fit include the acceptance of the COMPASS apparatus.

ditional Reggeon exchanges are needed in the fast-$\eta$ amplitudes. Given that the backward-peak events, fast-$\pi$, are well-reproduced, we do not consider contributions by the subleading $f_2'$.

We therefore include the subleading $a_2'$ and the exotic $\pi_1$ as additional top exchanges (see **??**), adding the $a_2' f_2$, $a_2'\mathbb{P}$, $\pi_1 f_2$, and $\pi_1\mathbb{P}$ amplitudes to the base model. The $\pi_1$ trajectory is distinguished by its negative signature (odd spin) while all other trajectories considered have positive signature (even spin); its inclusion thus tests the role of a negative-signature exchange. Details of the trajectories are given in the End Matter. For diagnostics, we also performed the analysis in bins of $m_{\eta\pi}$ fitted independently, verifying that the parameters remain stable and compatible with the global best fit. Results are presented in the Supplemental Material [52].

The minimal fit, which contains only the base model, is compared with fits that add the $a_2'$ exchange, the $\pi_1$ exchange, or both, and significances are extracted from the resulting ENLLs using Wilks' theorem [53] as explained in the End Matter. In this way, the data can select the preferred Regge signature. In addition, we scan the parameters of the $a_2'$ and $\pi_1$ trajectories over wide, overlapping ranges. The results are summarized in Table I. The reported values correspond to the closest likelihoods obtained and therefore represent minimum significances. The additional exchanges are required at more than $11\,\sigma$ ($10\,\sigma$) in the $\eta\pi^-$ ($\eta'\pi^-$) channel. The negative-signature

TABLE I. Minimal significance studies. The base model contains only the leading ordinary exchanges.

| Hypotheses | | Significance | |
|---|---|---|---|
| $H_0$ | $H_1$ | $\eta\pi^-$ | $\eta'\pi^-$ |
| Base | Base + $a_2'$ | $11.0\,\sigma$ | $10.1\,\sigma$ |
| Base | Base + $\pi_1$ | $12.8\,\sigma$ | $11.7\,\sigma$ |
| Base | Base + $a_2'$ + $\pi_1$ | $15.4\,\sigma$ | $12.2\,\sigma$ |
| Base + $a_2'$ | Base + $a_2'$ + $\pi_1$ | $9.9\,\sigma$ | $5.5\,\sigma$ |
| Base + $\pi_1$ | Base + $a_2'$ + $\pi_1$ | $2.2\,\sigma$ | disfavored |

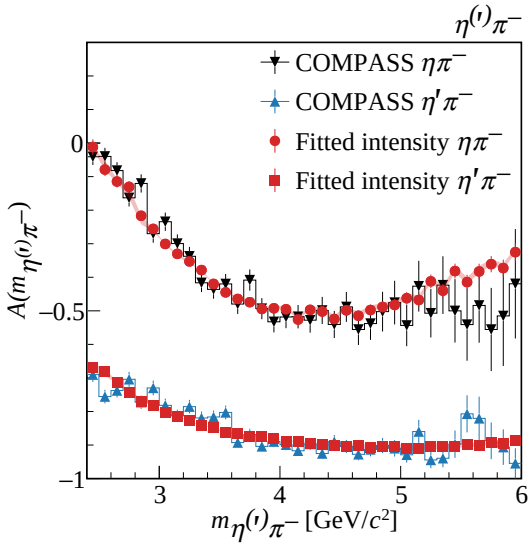


FIG. 5. Forward-backward asymmetry for both channels. Note the large uncertainties at the highest mass bins due to the small amount of forward events (see Fig. 1.) Systematic uncertainties are provided as a band. Data and fit include the acceptance of the COMPASS apparatus.

$\pi_1$ Reggeon in the top exchange is needed to describe the data within uncertainties, as illustrated in Fig. 3: relative to a fit with the base model and the $a_2'$ exchange, adding the $\pi_1$ has a significance of $9.9\,\sigma$ ($5.5\,\sigma$) for the $\eta\pi^-$ ($\eta'\pi^-$) channel. Best-fit parameters, their statistical and systematic uncertainties, and a detailed comparison between model fits and data are provided in the Supplemental Material [52].

As shown in Fig. 4, the bottom-$\mathbb{P}$ exchange dominates over the bottom-$f_2$, except at the smallest $t_p$ where the two are comparable, confirming the relevance of the $f_2$ exchange suggested in Ref. [43]. Future analyses of diffractive processes at center-of-mass energies of tens of GeV should therefore assess contributions beyond $\mathbb{P}$. The slopes extracted for the proton-$\mathbb{P}$-proton vertex form factor agree within uncertainties between the two channels and are consistent with the TOTEM-CMS result [54].

Both $\eta^{(\prime)}\pi^-$ forward-backward asymmetries differ significantly from zero, demonstrating the presence of odd

exotic waves beyond the resonance region. The asymmetry is well reproduced (Fig. 5), confirming that the DR amplitude is the dominant production mechanism for forward and backward events above the resonance region. A nonsignificant deviation between fit and data appears at the highest energies, where the dynamics is dominated by the top $\mathbb{P}$, and might require a small correction of the $\mathbb{P}$ amplitude, as shown in the Supplemental Material [52], were it to be confirmed by further statistics.

*Summary.*— We report the first observation of an exotic Reggeon exchange, established at $9.9\,\sigma$ ($5.5\,\sigma$) in the $\eta\pi^-$ ($\eta'\pi^-$) channel and most plausibly identified with the $\pi_1(1600)$. This exotic trajectory contributes at leading order alongside the Pomeron and is required to describe the data. The dynamics generating exotic waves is therefore richer than previously recognized: hybrid mesons appear here not only as produced resonances but as exchanged trajectories, opening a complementary window on gluonic excitations in QCD. These findings motivate analogous measurements at GlueX, whose polarized photon beam and access to $\eta^{(\prime)}\pi^0$ final states [55] would probe the large forward-backward asymmetry predicted in $\eta^{(\prime)}\pi^0$ photoproduction [56], a channel in which Pomeron exchange is forbidden and the exotic contribution can therefore be isolated. The analysis also opens the way to incorporating analyticity constraints in low-energy partial-wave extractions [57], sharpening the determination of hybrid-meson parameters. Additionally, we find a substantial contribution of $f_2$ bottom exchange over a wide angular range. For the COMPASS kinematics, this contribution is subdominant to the favored Pomeron exchange [58], which is conventionally associated in QCD with gluonic degrees of freedom carrying vacuum quantum numbers [59–61]. Quantifying such subdominant exchanges is also essential for diffractive parton distribution functions [62], Odderon searches [63], and diffractive production at the future Electron-Ion Collider [64, 65].

*Acknowledgments.*— We gratefully acknowledge the support of the CERN management and staff and the skill and effort the technicians of our collaborating institutes. This work was made possible by the financial support of our funding agencies: The Higher Education and Science Committee of the Republic of Armenia (Armenia); MEYS, Grants LM2023040, CZ.02.01.01/00/22_008/0004632 “FORTE” (Czech Republic); BMBF – Bundesministerium für Bildung und Forschung (Germany); the B. Sen fund (India); the Israel Academy of Sciences and Humanities (Israel); MEXT and JSPS, Grants 18002006, 20540299, 18540281 and 26247032, the Daiko and Yamada Foundations (Japan); NCN, Grant 2020/37/B/ST2/01547 (Poland); FCT, Grants DOI 10.54499/CERN/FIS-PAR/0022/2019 and DOI 10.54499/CERN/FIS-PAR/0016/2021 (Portugal); the Ministry of Science and Technology (Taiwan); and the National Science Foundation, Grant No. PHY-1506416 (USA), the Excellence Cluster Universe which is funded by the Deutsche Forschungsgemeinschaft (DFG, German Research Foundation), the Excellence Cluster ORIGINS which is funded by the DFG under Germany’s Excellence Strategy – EXC 2094 – 390783311, the Computational Center for Particle and Astrophysics (C2PAP), and the Leibniz Supercomputer Center (LRZ), the U.S. Department of Energy, Office of Science, Office of Nuclear Physics under Contract No. 89243126CSC00021, U.S. Department of Energy contracts DE-FG02-87ER40365, DE-SC0011090, and DE-SC0023598; Simons Foundation award Simons Collaboration on Confinement and QCD StringsMPS-QCD-00994314 and by MIT; Projects CNS2022-136085, CEX2024-001451-M (Unidad de Excelencia “María de Maeztu”), PID2020-118758GB-I00, and PID2023-147112NB-C21, all financed by MICIU/AEI/10.13039/501100011033/ and FEDER, UE; the Beatriu de Pinós program by AGAUR, Grant No. BP 2024 00189; the COST Action CA24159 “Structure and Spectroscopy of Hadrons Research Project (SHARP)”, supported by COST (European Cooperation in Science and Technology); and the European Union’s Horizon 2020 research and innovation programme under Grant Agreement STRONG–2020—No. 824093.

[a] Corresponding author
[b] Supported by the European Union’s Horizon 2020 research and innovation programme under grant agreement STRONG–2020 - No 824093
[c] Also at Dept. of Physics, Pusan National University, Busan 609-735, Republic of Korea; Also at Physics Dept., Brookhaven National Laboratory, Upton, NY 11973, USA
[d] Deceased
[e] Present address: NISER, Centre for Medical and Radiation Physics, Bubaneswar, India
[f] Retired from Ludwig-Maximilians-Universität, 80539 München, Germany; Supported by the DFG cluster of excellence ‘Origin and Structure of the Universe’ (www.universe-cluster.de) (Germany)
[g] Also at INFN TIFPA, 38123 Trento, Italy; Also at Università di Trento, 38123 Trento, Italy
[h] Also at KEK, 1-1 Oho, Tsukuba, Ibaraki 305-0801, Japan
[i] Supported by the Max Planck Institute for Physics, 85748 Garching, Germany
[j] Also at Dept. of Physics, National Kaohsiung Normal University, Kaohsiung County 824, Taiwan
[k] Also at Institut für Theoretische Physik, Universität Tübingen, 72076 Tübingen, Germany
[l] Also at RIKEN Nishina Center for Accelerator-Based Science, Wako, Saitama 351-0198, Japan
[m] Also at University of Eastern Piedmont, 15100 Alessan-

dria, Italy; Supported by the Funds for Research 2019-22 of the University of Eastern Piedmont
[n] Corresponding author; pekeler@hiskp.uni-bonn.de
[o] Also at Chubu University, Kasugai, Aichi 487-8501, Japan
[p] Also at Fairmont State University, Department of Natural Sciences, 1201 Locust Ave, Fairmont, West Virginia 26554, USA
[q] Corresponding author; cefera@ccia.uned.es
[r] Also a COMPASS collaboration member

[1] M. R. Shepherd, J. J. Dudek, and R. E. Mitchell, Nature **534**, 487 (2016).
[2] N. Brambilla *et al.*, Eur. Phys. J. **C74**, 2981 (2014), arXiv:1404.3723 [hep-ph].
[3] S. Navas *et al.* (Particle Data Group), Phys. Rev. **D110**, 030001 (2024).
[4] A. Esposito, A. Pilloni, and A. D. Polosa, Phys. Rept. **668**, 1 (2017), arXiv:1611.07920 [hep-ph].
[5] R. F. Lebed, R. E. Mitchell, and E. S. Swanson, Prog. Part. Nucl. Phys. **93**, 143 (2017), arXiv:1610.04528 [hep-ph].
[6] F.-K. Guo, C. Hanhart, U.-G. Meißner, Q. Wang, Q. Zhao, and B.-S. Zou, Rev. Mod. Phys. **90**, 015004 (2018), arXiv:1705.00141 [hep-ph].
[7] S. L. Olsen, T. Skwarnicki, and D. Zieminska, Rev. Mod. Phys. **90**, 015003 (2018), arXiv:1708.04012 [hep-ph].
[8] N. Brambilla, S. Eidelman, C. Hanhart, A. Nefediev, C.-P. Shen, C. E. Thomas, A. Vairo, and C.-Z. Yuan, Phys. Rept. **873**, 1 (2020), arXiv:1907.07583 [hep-ex].
[9] B. Ketzer, B. Grube, and D. Ryabchikov, Prog. Part. Nucl. Phys. **113**, 103755 (2019), arXiv:1909.06366 [hep-ex].
[10] T. Barnes and F. Close, Phys. Lett. **B116**, 365 (1982).
[11] T. Barnes, F. Close, F. de Viron, and J. Weyers, Nucl. Phys. **B224**, 241 (1983).
[12] D. Horn and J. Mandula, Phys. Rev. **D17**, 898 (1978).
[13] M. S. Chanowitz and S. R. Sharpe, Nucl. Phys. **B222**, 211 (1983), [Erratum: Nucl. Phys. B228, 588 (1983)].
[14] N. Isgur and J. E. Paton, Phys. Rev. **D31**, 2910 (1985).
[15] E. Klempt and A. Zaitsev, Phys. Rept. **454**, 1 (2007), arXiv:0708.4016 [hep-ph].
[16] J. J. Dudek and R. G. Edwards, Phys. Rev. **D85**, 054016 (2012), arXiv:1201.2349 [hep-ph].
[17] B. Ketzer, in *Proceedings, 6th International Conference on Quarks and Nuclear Physics (QNP 2012): Palaiseau, France, April 16-20, 2012*, Vol. QNP2012 (2012) p. 025, arXiv:1208.5125 [hep-ex].
[18] C. A. Meyer and E. S. Swanson, Prog. Part. Nucl. Phys. **82**, 21 (2015), arXiv:1502.07276 [hep-ph].
[19] F. Gross *et al.*, Eur. Phys. J. **C83**, 1125 (2023), arXiv:2212.11107 [hep-ph].
[20] D. R. Thompson *et al.* (E852), Phys. Rev. Lett. **79**, 1630 (1997), arXiv:hep-ex/9705011 [hep-ex].
[21] S. U. Chung *et al.* (E852), Phys. Rev. **D60**, 092001 (1999), arXiv:hep-ex/9902003.
[22] A. Abele *et al.* (Crystal Barrel), Phys. Lett. **B423**, 175 (1998).
[23] G. M. Beladidze *et al.* (VES), Phys. Lett. **B313**, 276 (1993).
[24] E. I. Ivanov *et al.* (E852), Phys. Rev. Lett. **86**, 3977 (2001), arXiv:hep-ex/0101058 [hep-ex].
[25] P. Abbon *et al.* (COMPASS), Nucl.Instrum.Meth. **A779**, 68 (2015), arXiv:1410.1797 [physics.ins-det].
[26] C. Adolph *et al.* (COMPASS), Phys. Lett. **B740**, 303 (2015), [Erratum: Phys. Lett. **B811**, 135913 (2020)], arXiv:1408.4286 [hep-ex].
[27] A. Rodas *et al.* (JPAC), Phys. Rev. Lett. **122**, 042002 (2019), arXiv:1810.04171 [hep-ph].
[28] P. Lacock, C. Michael, P. Boyle, and P. Rowland (UKQCD), Phys. Lett. **B401**, 308 (1997), arXiv:hep-lat/9611011 [hep-lat].
[29] C. W. Bernard *et al.* (MILC), Phys. Rev. **D56**, 7039 (1997), arXiv:hep-lat/9707008.
[30] J. J. Dudek, R. G. Edwards, P. Guo, and C. E. Thomas (Hadron Spectrum), Phys. Rev. **D88**, 094505 (2013), arXiv:1309.2608 [hep-lat].
[31] A. P. Szczepaniak and E. S. Swanson, Phys. Rev. **D65**, 025012 (2002), arXiv:hep-ph/0107078 [hep-ph].
[32] A. P. Szczepaniak and P. Krupinski, Phys. Rev. **D73**, 116002 (2006), arXiv:hep-ph/0604098 [hep-ph].
[33] P. Guo, A. P. Szczepaniak, G. Galatà, A. Vassallo, and E. Santopinto, Phys. Rev. **D78**, 056003 (2008), arXiv:0807.2721 [hep-ph].
[34] M. Albrecht *et al.* (Crystal Barrel), Eur. Phys. J. **C80**, 453 (2020), arXiv:1909.07091 [hep-ex].
[35] B. Kopf, M. Albrecht, H. Koch, M. Küßner, J. Pychy, X. Qin, and U. Wiedner, Eur. Phys. J. **C81**, 1056 (2021), arXiv:2008.11566 [hep-ph].
[36] A. J. Woss, J. J. Dudek, R. G. Edwards, C. E. Thomas, and D. J. Wilson (Hadron Spectrum), Phys. Rev. **D103**, 054502 (2021), arXiv:2009.10034 [hep-lat].
[37] P. D. B. Collins, *An Introduction to Regge Theory and High-Energy Physics*, Cambridge Monographs on Mathematical Physics (Cambridge Univ. Press, Cambridge, UK, 2009).
[38] D. Winney and A. P. Szczepaniak, arXiv:2512.21805 [hep-ph] (2025).
[39] P. Abbon *et al.* (COMPASS), Nucl. Instrum. Meth. **A577**, 455 (2007), arXiv:hep-ex/0703049.
[40] P. Abbon *et al.* (COMPASS), Nucl. Instrum. Meth. **A779**, 69 (2015), arXiv:1410.1797 [physics.ins-det].
[41] H. Pekeler, *Production of $\eta\pi^-$ and $\eta'\pi^-$ Final States in High Energy $\pi^-p$ Scattering at COMPASS*, Ph.D. thesis, Bonn Universität (2025).
[42] K. Gottfried and J. D. Jackson, Nuovo Cim. **33**, 309 (1964).
[43] L. Bibrzycki, C. Fernández-Ramírez, V. Mathieu, M. Mikhasenko, M. Albaladejo, A. N. H. Blin, A. Pilloni, and A. P. Szczepaniak (JPAC), Eur. Phys. J. **C81**, 647 (2021), [Erratum: Eur. Phys. J. C81, 915 (2021)], arXiv:2104.10646 [hep-ph].
[44] A. Bialas and S. Pokorski, Nucl. Phys. **B10**, 399 (1969).
[45] M. Shi, I. V. Danilkin, C. Fernández-Ramírez, V. Mathieu, M. R. Pennington, D. Schott, and A. P. Szczepaniak, Phys. Rev. **D91**, 034007 (2015), arXiv:1411.6237 [hep-ph].
[46] R. Brower, C. E. DeTar, and J. Weis, Phys. Rept. **14**, 257 (1974).
[47] J. H. Weis, Phys. Rev. **D6**, 2823 (1972).
[48] T. Shimada, A. D. Martin, and A. C. Irving, Nucl. Phys. **B142**, 344 (1978).
[49] T. C. Szameitat, *New geant4-based Monte Carlo software for the COMPASS-II experiment at CERN*, Ph.D. thesis, Freiburg U. (2017).
[50] S. Agostinelli *et al.* (GEANT4), Nucl. Instrum. Meth. A **506**, 250 (2003).
[51] I. Antcheva *et al.*, Comput. Phys. Commun. **180**, 2499 (2009), arXiv:1508.07749 [physics.data-an].

[52] Supplemental material, at [URL will be inserted by publisher].

[53] S. S. Wilks, Annals Math. Statist. **9**, 60 (1938).

[54] A. Hayrapetyan *et al.* (TOTEM, CMS), Phys. Rev. **D109**, 112013 (2024), arXiv:2401.14494 [hep-ex].

[55] S. Adhikari *et al.* (GlueX), Nucl. Instrum. Meth. **A987**, 164807 (2021), arXiv:2005.14272 [physics.ins-det].

[56] G. Montaña *et al.*, Phys. Lett. **B872**, 140101 (2026), arXiv:2510.14549 [hep-ph].

[57] V. Mathieu, J. Nys, A. Pilloni, C. Fernández-Ramírez, A. Jackura, M. Mikhasenko, V. Pauk, A. P. Szczepaniak, and G. Fox, EPL **122**, 41001 (2018), arXiv:1708.07779 [hep-ph].

[58] F. Haas, *Two-Dimensional Partial-Wave Analysis of Exclusive 190 GeV $\pi^- p$ Scattering into the $\pi^-\pi^-\pi^+$ Final State at COMPASS (CERN)*, Ph.D. thesis, Technische Universität München (2013).

[59] E. A. Kuraev, L. N. Lipatov, and V. S. Fadin, Sov. Phys. JETP **45**, 199 (1977).

[60] I. I. Balitsky and L. N. Lipatov, Sov. J. Nucl. Phys. **28**, 822 (1978).

[61] A. Donnachie and P. V. Landshoff, Nucl. Phys. **B311**, 509 (1989).

[62] A. Aktas *et al.* (H1), J. High Energy Phys. **10**, 042, arXiv:0708.3217 [hep-ex].

[63] V. M. Abazov *et al.* (D0, TOTEM), Phys. Rev. Lett. **127**, 062003 (2021), arXiv:2012.03981 [hep-ex].

[64] R. Abdul Khalek *et al.*, Nucl. Phys. **A1026**, 122447 (2022), arXiv:2103.05419 [physics.ins-det].

[65] D. P. Anderle *et al.*, Front. Phys. (Beijing) **16**, 64701 (2021), arXiv:2102.09222 [nucl-ex].

## END MATTER

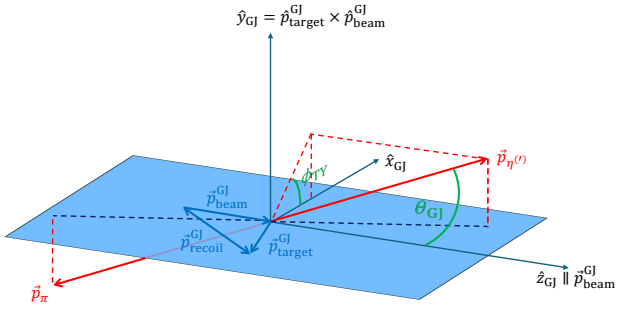


FIG. 6. Gottfried-Jackson reference frame. The precise definition of the vectors can be found in the text.

*Kinematics.*— The data is analyzed in the Gottfried-Jackson (GJ) reference frame [42], where the $\eta^{(\prime)}\pi^-$ system is at rest and the $\pi^-$ beam defines the $z$-axis. The production plane is perpendicular to $\vec{p}^{\rm GJ}_{\rm target} \times \vec{p}^{\rm GJ}_{\rm beam}$, see Fig. 6. Given that $\vec{p}^{\rm GJ}_{\eta^{(\prime)}} + \vec{p}^{\rm GJ}_{\pi} = \vec{0}$ the momenta are related as follows:

$$\begin{aligned}
&\vec{p}^{\rm GJ}_{\rm beam} + \vec{p}^{\rm GJ}_{\rm target} = \vec{p}^{\rm GJ}_{\rm recoil},\\
&\vec{p}^{\rm GJ}_{\rm recoil} \times \vec{p}^{\rm GJ}_{\rm beam} = \left(\vec{p}^{\rm GJ}_{\rm beam} + \vec{p}^{\rm GJ}_{\rm target}\right) \times \vec{p}^{\rm GJ}_{\rm beam},\\
&\vec{p}^{\rm GJ}_{\rm target} \times \vec{p}^{\rm GJ}_{\rm beam} = \vec{p}^{\rm GJ}_{\rm recoil} \times \vec{p}^{\rm GJ}_{\rm beam}.
\end{aligned}$$

We define the characteristic angles in the $\eta^{(\prime)}\pi^-$ system, *i.e.* $\theta_{\rm GJ}$ is the polar angle between the $\eta^{(\prime)}$ and the $z$-axis, $\phi_{\rm TY}$ is the azimuthal angle between the projection of the $\vec{p}^{\rm GJ}_{\eta}$ on the $xy$ plane and the $x$ axis, and $\epsilon$ is the angle between the recoil proton and the $\pi^-$ beam. Each event four-momenta $\zeta_k$ is characterized by the Mandelstam variables:

$$\begin{aligned}
s &= (p_\eta + p_\pi + p_{\rm recoil})^2\,, \quad & s_{\eta\pi} &= (p_\eta + p_\pi)^2\,,\\
s_{\eta p} &= (p_\eta + p_{\rm recoil})^2\,, \quad & s_{\pi p} &= (p_\pi + p_{\rm recoil})^2\,,\\
t_p &= (p_\eta + p_\pi - p_{\rm beam})^2\,, \quad & t_\eta &= (p_\eta - p_{\rm beam})^2\,,\\
t_\pi &= (p_\pi - p_{\rm beam})^2\,,
\end{aligned}$$

which can be computed in any reference frame, in particular GJ.

*Double-Regge amplitude.*— The double-Regge mechanism shown in **??** dominates in the kinematic regime given by $s, s_{12}, s_{2p} \to \infty$ with fixed $t_1$ and $t_p$, and finite $\kappa^{-1} \equiv s/(\beta s_{12} s_{2p})$ [46]. The intensity distribution in terms of the double-Regge amplitudes reads:

$$\begin{aligned}
I(\{c,b\};\zeta_k) =& \left|\sum_i c_i\, A_i(\{b\};\zeta_k)\right|^2\\
=& \big|c_{\pi_1 f_2}\, A_{\pi_1 f_2}(\{b\};\zeta_k) + c_{\pi_1 \mathbb{P}}\, A_{\pi_1 \mathbb{P}}(\{b\};\zeta_k)\\
&+ c_{a_2 f_2}\, A_{a_2 f_2}(\{b\};\zeta_k) + c_{a_2 \mathbb{P}}\, A_{a_2 \mathbb{P}}(\{b\};\zeta_k)\\
&+ c_{a'_2 f_2}\, A_{a'_2 f_2}(\{b\};\zeta_k) + c_{a'_2 \mathbb{P}}\, A_{a'_2 \mathbb{P}}(\{b\};\zeta_k)\\
&+ c_{f_2 f_2}\, A_{f_2 f_2}(\{b\};\zeta_k) + c_{f_2 \mathbb{P}}\, A_{f_2 \mathbb{P}}(\{b\};\zeta_k)\\
&+ \; c_{\mathbb{P} f_2}\, A_{\mathbb{P} f_2}(\{b\};\zeta_k) + c_{\mathbb{P}\mathbb{P}}\, A_{\mathbb{P}\mathbb{P}}(\{b\};\zeta_k)\,\big|^2\,,
\end{aligned}$$

where $\zeta_k$ stands for the four-momenta of each event. Each amplitude is given a real valued strength parameter $c_i$, that is fitted to the event distribution. The amplitudes include form factors $F_i(t) = \exp[b_i t]$ at the top and bottom vertices which are also fitted. Hence, each amplitude contains two form factors, which effectively absorb any contribution from the middle vertex. In doing so, we end up with seven slope parameters, namely: $b_{\pi_1}$ associated to the exotic $\pi\pi_1\eta$ vertex, $b_{a_2}$ to the $\pi a_2\eta$ vertex, $b_{a'_2}$ to the $\pi a'_2\eta$ vertex, $b_{f_2}$ to the $\pi f_2\pi$ vertex, $b_{\mathbb{P}}$ to the $\pi\mathbb{P}\pi$ vertex, $b_f$ to the $pf_2p$ vertex, and $b_P$ to the $p\mathbb{P}p$ vertex. The fast $\eta$ amplitudes read:

$$A_{nm}(b_n, b_m; \zeta_k) = F_n(t_\eta)\, F_m(t_p)\, T\left(\alpha_n(t_\eta), \alpha_m(t_p); s_{\pi p}\right),$$

where $n = \pi_1$, $a_2$ or $a'_2$ and $m = f_2$ or $\mathbb{P}$ ($m = f$ or $P$) when referring to the exchange (vertex) and the fast $\pi$ amplitudes read:

$$A_{nm}(b_n, b_m; \zeta_k) = F_n(t_\pi)\, F_m(t_p)\, T\left(\alpha_n(t_\pi), \alpha_m(t_p); s_{\eta p}\right),$$

where $n = f_2$ or $\mathbb{P}$, $m$ as in the fast-$\eta$ diagram, and $T$ is the generic amplitude:

$$\begin{aligned}
T(\alpha_n, \alpha_m; s_{2p}) =& K\, \Gamma(1-\alpha_n)\, \Gamma(1-\alpha_m)\\
&\times \frac{s_0}{s} \left(\frac{s_{\eta\pi}}{s_0}\right)^{\alpha_n} \left(\frac{s_{2p}}{s_0}\right)^{\alpha_m}\\
&\times \left[\frac{\xi_n \xi_{mn}}{\kappa^{\alpha_n}} V(\alpha_n, \alpha_m; \kappa)\right.\\
&+ \left.\frac{\xi_m \xi_{nm}}{\kappa^{\alpha_m}} V(\alpha_m, \alpha_n; \kappa)\right],
\end{aligned}$$

with

$$K = 4\, m_{\eta\pi} \left|\vec{p}^{\rm GJ}_{\eta}\right| \left|\vec{p}^{\rm GJ}_{\rm beam}\right| \left|\vec{p}^{\rm GJ}_{\rm recoil}\right| \sin\epsilon\, \sin\theta_{\rm GJ}\, \sin\phi_{\rm TY},$$

and

$$\xi_n = \frac{\tau_n + e^{-i\pi\alpha_n}}{2}, \quad \xi_{nm} = \frac{\tau_n \tau_m + e^{-i\pi(\alpha_n - \alpha_m)}}{2},$$

where $\tau_n$ and $\tau_m$ are the signatures of the trajectories and

$$V(\alpha_1, \alpha_2; \kappa) = \frac{\Gamma(\alpha_1 - \alpha_2)}{\Gamma(1-\alpha_2)}\, {}_1F_1\left(1-\alpha_1, 1-\alpha_1+\alpha_2; -\kappa\right),$$

TABLE II. Linear Regge trajectories $\alpha(t) = \alpha_0 + \alpha' t$ used in our analysis from Ketzer, Grube and Ryabchikov (KGR) [9] and the JPAC collaboration in [43]. $\alpha'$ is given in units of $c^4\,\mathrm{GeV}^{-2}$. The $\mathbb{P}$ trajectory is taken from the Review of Particle Physics [3]. The exotic $\pi_1$ and ordinary $a_2'$ trajectory parameters are varied within the ranges provided.

| Trajectory | Signature | KGR | JPAC |
|---|---|---|---|
| $\alpha_{a_2}(t)$ | $+1$ | $0.44 + 0.917\,t$ | $0.53 + 0.90\,t$ |
| $\alpha_{f_2}(t)$ | $+1$ | $0.44 + 0.917\,t$ | $0.47 + 0.89\,t$ |
| $\alpha_{\mathbb{P}}(t)$ | $+1$ | $1.08 + 0.25\,t$ | |
| $\alpha_{a_2'}(t)$ | $+1$ | $[-0.66, -0.46] + [0.817, 1.017]\,t$ | |
| $\alpha_{\pi_1}(t)$ | $-1$ | $[-0.94, -0.54] + [\ 0.48,\ \ 0.88]\,t$ | |

where ${}_1F_1$ is the hypergeometric function of the first kind, with $\beta = 0.8\,c^4\,\mathrm{GeV}^{-2}$ [43]. The assumed Regge trajectories are linear and provided in Table II.

*Event fitting.*— The Monte Carlo accepted intensity is given by:

$$N(\{c,b\}) = \sum_{k=1}^{N_{\mathrm{acc}}} I(\{c,b\};\zeta_k) = \sum_{k=1}^{N_{\mathrm{acc}}} \left| \sum_i c_i A_i(\{b\};\zeta_k) \right|^2 ,$$

where $N_{\mathrm{acc}}$ stands for the number of accepted events. The Monte Carlo samples that describe the $\eta^{(\prime)}\pi^-$ final state are uniformly distributed in phase space. Each event is propagated through the COMPASS Monte Carlo simulation framework `TGEANT` [49], and reconstructed and selected in the same way as the COMPASS real data events. The parameters are determined by fitting to the experimental events using the extended negative log-likelihood (ENLL) [9]:

$$\mathrm{ENLL}(\{c,b\}) = N(\{c,b\}) - \sum_{k=1}^{N_{\mathrm{m}}} \ln I(\{c,b\};\zeta_k),$$

with $N_{\mathrm{m}}$ the number of measured events. The extended negative log-likelihood takes into account that the total intensity is a fixed quantity. The fit and the uncertainties are computed using `ROOT`'s `TMinuit2` package [51]. To find the best fit we perform 20 attempts with initial parameters randomly seeded. The best fit values together with the uncertainties from `MINUIT` are provided in the Supplemental Material [52].

*Systematics and significance.*— To assess the impact of Regge-parameter variations, we performed fits using the KGR and JPAC parameterizations for the leading ordinary exchanges. The plots in the Letter correspond to the KGR fits and include systematic uncertainty bands obtained by varying the poorly established $a_2'$ and $\pi_1$ trajectories over wide ranges, see Table II. A thorough comparison is shown in the Supplemental Material [52]. In this way we produce a large set of fits which sample the systematic effects associated to the variations of the parameters of the leading, subleading and exotic trajectories, as well as the inclusion of the $a_2'$ and $\pi_1$ trajectories. We use this sample to asses the significance of including the $\pi_1$ and the $a_2'$ exchanges.

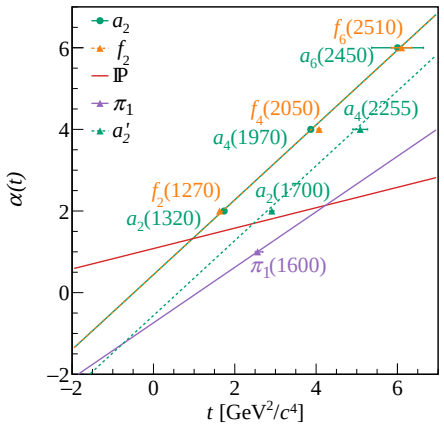


FIG. 7. Regge trajectories for the KGR parameters.

To quantify the statistical preference of extended models over the minimal hypothesis, we employ the likelihood-ratio test in the asymptotic regime described by Wilks' theorem [53]. For two nested models, we take the simpler model, with fewer parameters, as the null hypothesis $H_0$, and the more complex model, with additional parameters, as the alternative hypothesis $H_1$. We then define the test statistic:

$$q = -2 \ln \frac{\mathcal{L}_0}{\mathcal{L}_1} = 2\,(\mathrm{ENLL}_0 - \mathrm{ENLL}_1)\,,$$

where $\mathcal{L}_0$ and $\mathcal{L}_1$ denote the extended likelihoods evaluated under $H_0$ and $H_1$, respectively. Under the regularity conditions of Wilks' theorem (nested hypotheses), a sufficiently large sample size, and the absence of boundary effects—the test statistic $q$ follows a $\chi^2$ distribution with $k$ degrees of freedom under the null hypothesis, where $k$ is the difference in the number of free parameters between the two models. The corresponding $p$-value is computed as the probability of $\chi^2_k \geq q_{\mathrm{obs}}$, *i.e.* $p = P(\chi^2_k \geq q_{\mathrm{obs}})$, where $q_{\mathrm{obs}}$ is the value of the test statistic obtained from the observed data. This $p$-value is then translated into a Gaussian-equivalent significance, $Z = \Phi^{-1}(1-p)$, with $\Phi^{-1}$ denoting the inverse cumulative distribution function of the standard normal distribution. Within this framework, the resulting significance quantifies the degree to which the data disfavor the minimal model relative to the extended hypotheses, thereby providing a consistent criterion to assess whether the inclusion of additional parameters leads to a statistically justified improvement in the description of the data.

# Supplemental Material

## THREE-DIMENSIONAL EVENT DISTRIBUTIONS

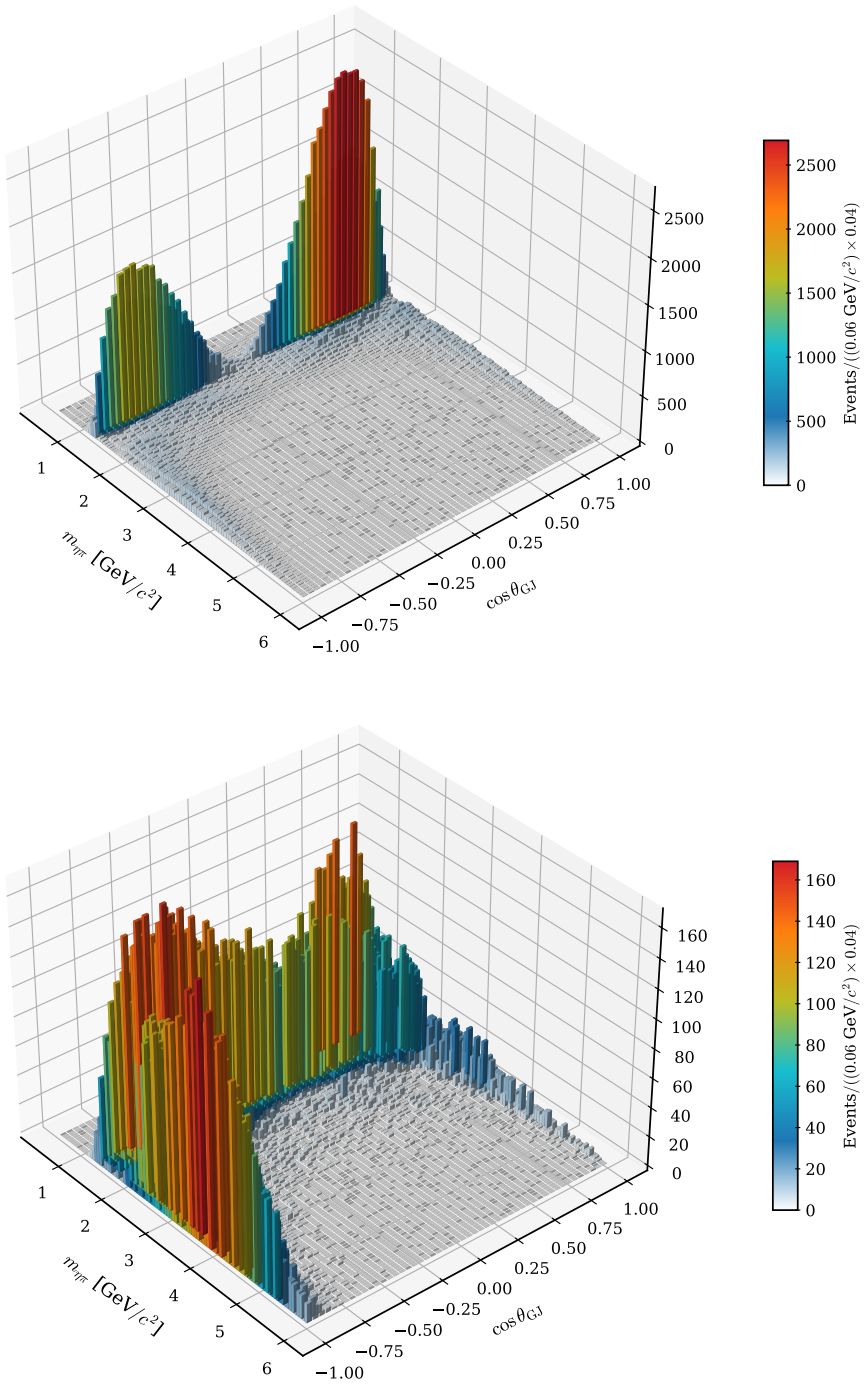


FIG. 8. Three-dimensional $\eta\pi^-$ (top) and $\eta'\pi^-$ (bottom) event distributions. The different structure of the events for both channels is very apparent. Note that the scales are different for each histogram and that the binning is different from the one presented in Fig. 1.

## FIT PARAMETERS

In this section we provide the model parameters and the associated uncertainties obtained by fitting the events in the double-Regge region, *i.e.* invariant mass range $[2.4, 6]$ GeV and angular range $|\cos\theta_{\rm GJ}| \geq 0.75$. The following sections provide a comprehensive comparison of the fits to the COMPASS data using two sets of parameters for the Regge trajectories provided in Table II. The comparison of the fits provide a sensible assessment of the systematics associated to the analysis. We provide eight fits for each channel:

- KGR: Fit with the leading ordinary exchanges using the KGR trajectories;
- KGR + $a_2'$: Fit with the ordinary leading and subleading $a_2'$ exchanges using the KGR trajectories;
- KGR + $\pi_1$: Fit with the ordinary leading and exotic $\pi_1$ exchanges using the KGR trajectories;
- KGR + $\pi_1$ + $a_2'$: Fit with the ordinary leading and subleading $a_2'$ and the exotic $\pi_1$ exchanges using the KGR trajectories;
- JPAC: Fit with the ordinary leading exchanges using the JPAC trajectories;
- JPAC + $a_2'$: Fit with the ordinary leading and subleading $a_2'$ exchanges using the JPAC trajectories;
- JPAC + $\pi_1$: Fit with the ordinary leading and exotic $\pi_1$ exchanges using the JPAC trajectories; and
- JPAC + $\pi_1$ + $a_2'$: Fit with the ordinary leading and subleading $a_2'$ and the exotic $\pi_1$ exchanges using the JPAC trajectories.

TABLE III. Linear Regge trajectories $\alpha(t) = \alpha_0 + \alpha' t$ used in our fits from Ketzer, Grube and Ryabchikov (KGR) [9] and the JPAC collaboration in [43]. Figure 7 shows the trajectories for the KGR parametrization. $\alpha'$ is given in units of $(c/\,\text{GeV})^2$. The $\mathbb{P}$ trajectory is taken from the Review of Particle Physics [3]. The $a_2'$ is the same as the $a_2$ shifted one unit. The $\pi_1$ trajectory is estimated from the mass of the $\pi_1(1600)$ and theoretical estimations of other potential members of the trajectory.

| Trajectory | Signature | KGR | JPAC |
|---|---|---|---|
| $\alpha_{a_2}(t)$ | $+1$ | $0.44 + 0.917\,t$ | $0.53 + 0.90\,t$ |
| $\alpha_{f_2}(t)$ | $+1$ | $0.44 + 0.917\,t$ | $0.47 + 0.89\,t$ |
| $\alpha_{\mathbb{P}}(t)$ | $+1$ | $1.08 + 0.25\,t$ | |
| $\alpha_{\pi_1}(t)$ | $-1$ | $-0.74 + 0.68\,t$ | |
| $\alpha_{a_2'}(t)$ | $+1$ | $-0.56 + 0.917\,t$ | $-0.47 + 0.90\,t$ |

Additionally we show fits in the $[4, 6]$ GeV invariant mass and angular $|\cos\theta_{\rm GJ}| \geq 0.75$ ranges using the ordinary leading exchanges for both KGR and JPAC parameterizations of the trajectories, named KGR-HE and JPAC-HE respectively, where HE stands for high energy. We note that for the $[2.4, 6]$ GeV range we fit $23,727$ events for the $\eta\pi^-$ channel and 21,421 for the $\eta'\pi$ while for the $[4, 6]$ GeV range we fit 4,970 events for the $\eta\pi^-$ channel and 6,388 for the $\eta'\pi$.

The fits performed using only the leading ordinary trajectories (base model) allow us to assess whether the data can be described solely by these contributions. We find that while the backward peak can indeed be reproduced, the forward peak cannot. This leads to the conclusion that contributions beyond the leading $a_2$ exchanges are required to properly account for the data. This need is further underscored by the behavior of the asymmetry. Moreover, we show that raising the lower-energy bound of the fitting window is insufficient: the inclusion of additional exchanges is unavoidable. JPAC *vs.* KGR fits provide an estimation of the impact of changing the parameters of the leading ordinary trajectories

TABLE IV. Values of the parameters for the best fit to $\eta\pi^-$ events using the KGR trajectories. $c_i$ parameters are dimensionless and $b_i$ parameters in units of $(\mathrm{GeV}/c)^{-2}$.

| | KGR-HE | KGR | KGR + $a_2'$ | KGR + $\pi_1$ | KGR + $\pi_1$ + $a_2'$ |
|---|---|---|---|---|---|
| Extended Log-Likelihood | 21618.3 | 84627.6 | 84544.2 | 84505 | 84479.3 |
| Strength parameters | | | | | |
| $c_{\pi_1 f_2}$ | — | — | — | −1.01(7) | −1.02(6) |
| $c_{\pi_1 \mathbb{P}}$ | — | — | — | 0.0069(32) | 0.0032(29) |
| $c_{a_2 f_2}$ | 0.069(7) | 0.120(4) | 0.100(4) | 0.076(4) | 0.074(4) |
| $c_{a_2 \mathbb{P}}$ | 0.0128(11) | 0.0129(4) | 0.0097(5) | 0.0105(4) | 0.0097(5) |
| $c_{a_2' f_2}$ | — | — | −0.68(22) | — | −26(7) |
| $c_{a_2' \mathbb{P}}$ | — | — | −0.0200(29) | — | 0.25(5) |
| $c_{f_2 f_2}$ | −0.111(28) | 0.242(21) | 0.246(25) | 0.240(22) | −0.330(31) |
| $c_{f_2 \mathbb{P}}$ | −0.0257(28) | 0.0149(10) | 0.0123(11) | 0.0129(9) | −0.0063(30) |
| $c_{\mathbb{P} f_2}$ | −0.0068(10) | 0.0119(18) | 0.0095(23) | 0.0102(21) | −0.0035(21) |
| $c_{\mathbb{P}\mathbb{P}}$ | 0.000 78(9) | −0.001 60(8) | −0.001 32(9) | −0.001 31(8) | 0.001 36(7) |
| Top Vertex Form Factors | | | | | |
| $b_{\pi_1}$ $(\pi\pi_1\eta)$ | — | — | — | −0.01(7) | −0.09(5) |
| $b_{a_2}$ $(\pi a_2\eta)$ | −0.16(6) | −0.136(21) | −0.15(4) | −0.215(23) | −0.192(23) |
| $b_{a_2'}$ $(\pi a_2'\eta)$ | — | — | 1.68(35) | — | 38(10) |
| $b_{f_2}$ $(\pi f_2\pi)$ | 0.25(14) | 1.63(15) | 1.25(14) | 1.21(13) | 1.43(12) |
| $b_{\mathbb{P}}$ $(\pi\mathbb{P}\pi)$ | 0.28(6) | 0.732(31) | 0.64(4) | 0.64(4) | 0.681(28) |
| Bottom Vertex Form Factors | | | | | |
| $b_f$ $(pf_2p)$ | 0.42(19) | 1.39(10) | 1.04(10) | 1.12(9) | 1.05(8) |
| $b_P$ $(p\mathbb{P}p)$ | 1.73(9) | 1.654(34) | 1.54(4) | 1.54(4) | 1.47(5) |

TABLE V. Values of the parameters for the best fit to $\eta\pi^-$ events using the JPAC trajectories. $c_i$ parameters are dimensionless and $b_i$ parameters in units of $(\mathrm{GeV}/c)^{-2}$.

| | JPAC-HE | JPAC | JPAC + $a_2'$ | JPAC + $\pi_1$ | JPAC + $\pi_1$ + $a_2'$ |
|---|---|---|---|---|---|
| Extended Log-Likelihood | 21617.3 | 84617.5 | 84550.9 | 84498.1 | 84462.6 |
| Strength parameters | | | | | |
| $c_{\pi_1 f_2}$ | — | — | — | −0.90(7) | −0.85(6) |
| $c_{\pi_1 \mathbb{P}}$ | — | — | — | 0.002(4) | −0.0006(33) |
| $c_{a_2 f_2}$ | 0.016(5) | 0.0667(27) | 0.0591(27) | 0.0421(26) | 0.0412(25) |
| $c_{a_2 \mathbb{P}}$ | 0.0145(16) | 0.010 65(27) | 0.0084(4) | 0.008 25(33) | 0.007 96(34) |
| $c_{a_2' f_2}$ | — | — | −0.35(14) | — | −14.2(34) |
| $c_{a_2' \mathbb{P}}$ | — | — | −0.0193(33) | — | 0.164(35) |
| $c_{f_2 f_2}$ | 0.002(18) | 0.184(18) | −0.192(18) | 0.192(19) | −0.224(23) |
| $c_{f_2 \mathbb{P}}$ | −0.036(4) | 0.0163(10) | −0.0129(11) | 0.0134(9) | −0.0110(13) |
| $c_{\mathbb{P} f_2}$ | −0.0059(7) | 0.0137(15) | −0.0112(17) | 0.0116(17) | −0.0091(22) |
| $c_{\mathbb{P}\mathbb{P}}$ | 0.000 80(9) | −0.001 89(9) | 0.001 59(10) | −0.001 52(9) | 0.001 55(8) |
| Top Vertex Form Factors | | | | | |
| $b_{\pi_1}$ $(\pi\pi_1\eta)$ | — | — | — | 0.17(12) | −0.04(6) |
| $b_{a_2}$ $(\pi a_2\eta)$ | −0.18(6) | −0.165(21) | −0.10(5) | −0.221(29) | −0.202(26) |
| $b_{a_2'}$ $(\pi a_2'\eta)$ | — | — | 1.4(4) | — | 31(9) |
| $b_{f_2}$ $(\pi f_2\pi)$ | 0.11(10) | 1.96(18) | 1.54(15) | 1.46(14) | 1.59(14) |
| $b_{\mathbb{P}}$ $(\pi\mathbb{P}\pi)$ | 0.25(5) | 0.801(30) | 0.72(4) | 0.706(35) | 0.717(33) |
| Bottom Vertex Form Factors | | | | | |
| $b_f$ $(pf_2p)$ | −0.70(30) | 1.61(13) | 1.27(12) | 1.38(11) | 1.32(10) |
| $b_P$ $(p\mathbb{P}p)$ | 2.32(14) | 1.770(33) | 1.67(4) | 1.61(4) | 1.59(4) |

TABLE VI. Values of the parameters for the best fit to $\eta'\pi^-$ events using the KGR trajectories. $c_i$ parameters are dimensionless and $b_i$ parameters in units of $(\,\mathrm{GeV}/c)^{-2}$.

| | KGR-HE | KGR | KGR + $a_2'$ | KGR + $\pi_1$ | KGR + $\pi_1$ + $a_2'$ |
|---|---|---|---|---|---|
| Extended Log-Likelihood | 28211.4 | 86871.3 | 86807.1 | 86792.1 | 86763.9 |
| Strength parameters | | | | | |
| $c_{\pi_1 f_2}$ | — | — | — | −1.45(18) | −1.26(10) |
| $c_{\pi_1 \mathbb{P}}$ | — | — | — | 0.087(29) | 0.041(18) |
| $c_{a_2 f_2}$ | 0.031(4) | 0.0511(27) | 0.0329(22) | 0.0172(31) | 0.0144(24) |
| $c_{a_2 \mathbb{P}}$ | 0.0036(6) | 0.006 57(35) | 0.003 34(28) | 0.0050(4) | 0.004 13(31) |
| $c_{a_2' f_2}$ | — | — | −1.67(33) | — | 0.036(9) |
| $c_{a_2' \mathbb{P}}$ | — | — | −0.041(5) | — | 0.002 80(34) |
| $c_{f_2 f_2}$ | −0.148(15) | −0.154(9) | 0.154(8) | 0.156(8) | 0.107(9) |
| $c_{f_2 \mathbb{P}}$ | −0.0076(17) | −0.0056(5) | 0.0052(5) | 0.0053(5) | 0.0100(6) |
| $c_{\mathbb{P} f_2}$ | −0.0047(7) | −0.0083(7) | 0.0076(6) | 0.0079(7) | 0.0086(6) |
| $c_{\mathbb{P}\mathbb{P}}$ | 0.000 45(4) | 0.000 79(5) | −0.000 68(5) | −0.000 72(5) | −0.000 66(5) |
| Top Vertex Form Factors | | | | | |
| $b_{\pi_1}$ $(\pi\pi_1\eta)$ | — | — | — | 2.88(33) | 2.00(22) |
| $b_{a_2}$ $(\pi a_2\eta)$ | −0.40(8) | 0.32(5) | −0.27(6) | −0.26(5) | −0.655(16) |
| $b_{a_2'}$ $(\pi a_2'\eta)$ | — | — | 5.2(4) | — | −0.674(13) |
| $b_{f_2}$ $(\pi f_2\pi)$ | 0.10(10) | 0.81(9) | 0.63(8) | 0.70(9) | 0.35(7) |
| $b_{\mathbb{P}}$ $(\pi\mathbb{P}\pi)$ | 0.12(5) | 0.381(33) | 0.313(33) | 0.341(33) | 0.317(35) |
| Bottom Vertex Form Factors | | | | | |
| $b_f$ $(pf_2p)$ | −0.11(10) | 0.19(9) | 0.06(8) | 0.15(8) | −0.05(8) |
| $b_P$ $(p\mathbb{P}p)$ | 1.25(8) | 1.48(5) | 1.41(5) | 1.41(5) | 1.47(5) |

TABLE VII. Values of the parameters for the best fit to $\eta'\pi^-$ events using the JPAC trajectories. $c_i$ parameters are dimensionless and $b_i$ parameters in units of $(\,\mathrm{GeV}/c)^{-2}$.

| | JPAC-HE | JPAC | JPAC + $a_2'$ | JPAC + $\pi_1$ | JPAC + $\pi_1$ + $a_2'$ |
|---|---|---|---|---|---|
| Extended Log-Likelihood | 28214 | 86874.3 | 86813.1 | 86792.7 | 86758.4 |
| Strength parameters | | | | | |
| $c_{\pi_1 f_2}$ | — | — | — | −0.38(4) | −1.40(15) |
| $c_{\pi_1 \mathbb{P}}$ | — | — | — | −0.0185(29) | 0.088(30) |
| $c_{a_2 f_2}$ | 0.0169(27) | 0.0261(20) | 0.0189(14) | 0.0265(23) | 0.0061(16) |
| $c_{a_2 \mathbb{P}}$ | 0.0028(4) | 0.005 52(29) | 0.002 75(24) | 0.003 71(33) | 0.003 37(21) |
| $c_{a_2' f_2}$ | — | — | −0.92(23) | — | 0.026(6) |
| $c_{a_2' \mathbb{P}}$ | — | — | −0.048(5) | — | 0.002 41(28) |
| $c_{f_2 f_2}$ | 0.117(12) | −0.116(7) | 0.121(7) | −0.135(8) | 0.084(7) |
| $c_{f_2 \mathbb{P}}$ | 0.0072(15) | −0.0058(5) | 0.0052(5) | −0.0042(6) | 0.0091(5) |
| $c_{\mathbb{P} f_2}$ | 0.0044(6) | −0.0079(6) | 0.0072(6) | −0.0074(7) | 0.0082(6) |
| $c_{\mathbb{P}\mathbb{P}}$ | −0.000 43(5) | 0.000 81(5) | −0.000 70(5) | 0.000 76(5) | −0.000 68(5) |
| Top Vertex Form Factors | | | | | |
| $b_{\pi_1}$ $(\pi\pi_1\eta)$ | — | — | — | −0.01(5) | 3.07(32) |
| $b_{a_2}$ $(\pi a_2\eta)$ | −0.48(13) | 0.31(6) | −0.27(6) | 0.92(12) | −0.683(15) |
| $b_{a_2'}$ $(\pi a_2'\eta)$ | — | — | 5.2(4) | — | −0.700(12) |
| $b_{f_2}$ $(\pi f_2\pi)$ | 0.13(10) | 0.81(9) | 0.67(8) | 0.81(10) | 0.36(7) |
| $b_{\mathbb{P}}$ $(\pi\mathbb{P}\pi)$ | 0.10(5) | 0.368(35) | 0.312(34) | 0.355(35) | 0.32(4) |
| Bottom Vertex Form Factors | | | | | |
| $b_f$ $(pf_2p)$ | −0.08(11) | 0.13(9) | 0.10(8) | 0.24(8) | 0.00(8) |
| $b_P$ $(p\mathbb{P}p)$ | 1.29(9) | 1.57(5) | 1.47(5) | 1.45(5) | 1.49(5) |

## MASS DEPENDENT VS. MASS INDEPENDENT STRENGTH COUPLINGS

We conducted several exploratory fits to assess the energy range of applicability of the double-Regge amplitude. In particular, we performed individual fits to the events in narrow invariant mass bins (*a.k.a.* mass dependent fits) obtaining the strength couplings $\{c\}$ for each bin. The form factors were fixed to the best mass-independent event fit. Regge theory constrains the energy dependence of the amplitude, hence, if the double-Regge amplitude is the correct description of the data, the mass dependent strength couplings $\{c\}$ should remain approximately constant, within uncertainties, throughout the energy range. In Figs. 9 and 11 –$\eta\pi^-$ and $\eta'\pi^-$, respectively–, we show the strength couplings $\{c\}$ of the leading ordinary exchanges for each bin compared to the mass-independent event fit in the whole invariant mass range $m_{\eta\pi} \in [2.4, 6]\,\mathrm{GeV}/c^2$ using the KGR $+ a_2' + \pi_1$ parametrization. Figures 10 and 12 display the same for the nonleading exchanges. We find that in that invariant mass range the mass-independence assumption holds and the double-Regge amplitude correctly describes the energy dependence of the data. We note that the relative strength of the parameters do not correspond to the relative strength of the contributions as these are affected by the vertex form factors and the inherent strength of the specific diagram.

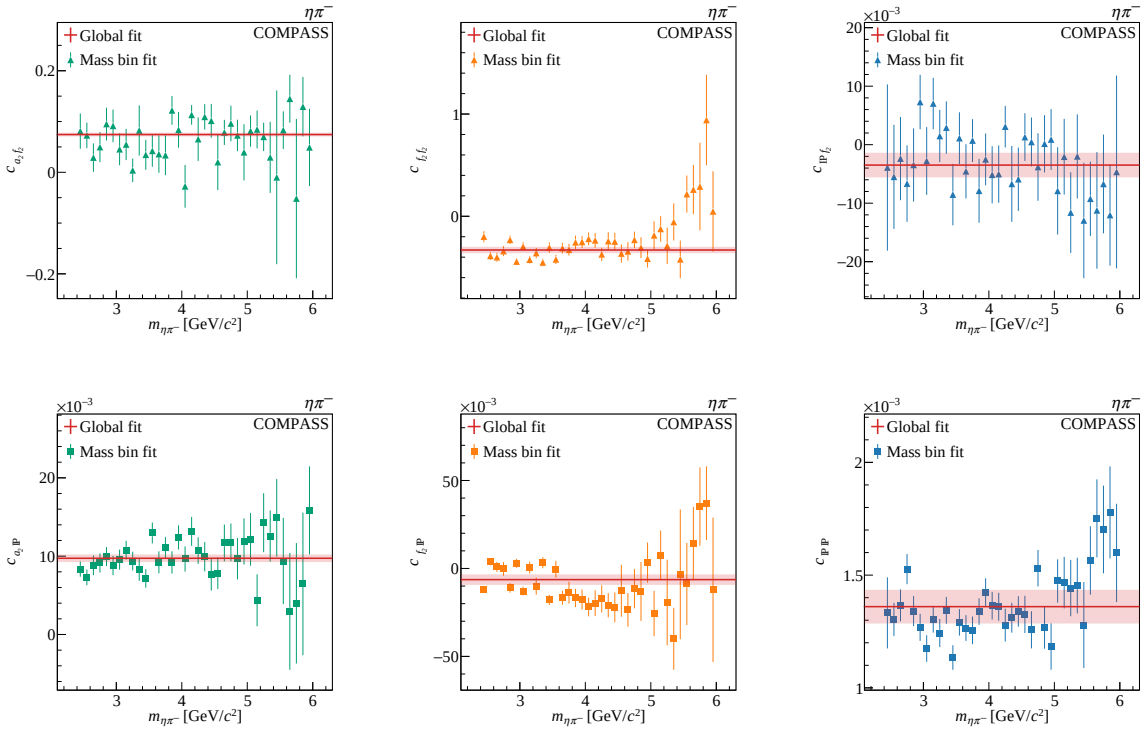


FIG. 9. $\eta\pi^-$ strength parameters $\{c\}$ of the KGR $+ a_2' + \pi_1$ fit for the leading ordinary exchanges. In red we display the best fit parameters to the data, and their uncertainties, in the double-Regge region shown in the Letter. The data points correspond to the event fits in a given invariant mass bin.

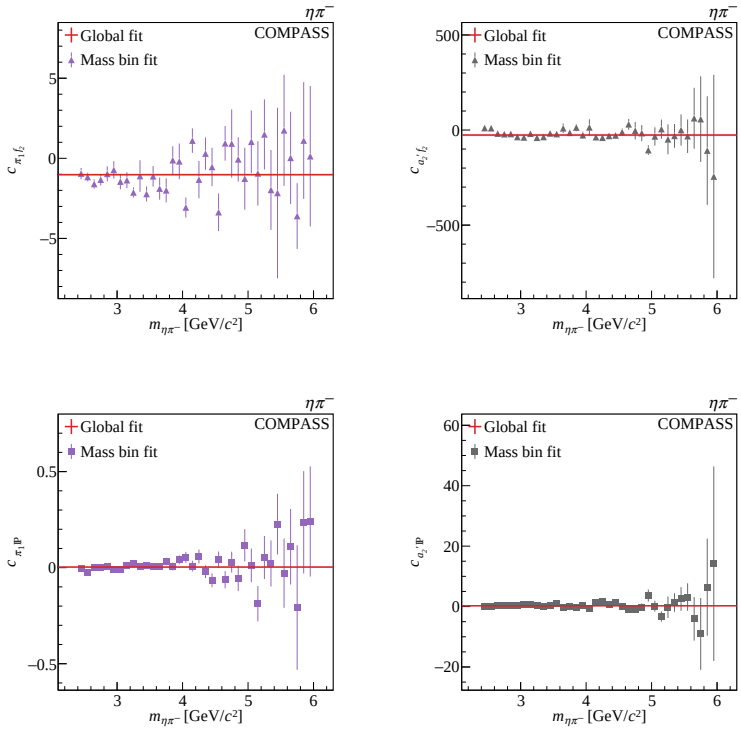


FIG. 10. $\eta\pi^-$ strength parameters $\{c\}$ of the KGR + $a_2' + \pi_1$ fit for the subleading $a_2'$ and exotic $\pi_1$ exchanges. Conventions as in Fig. 9.

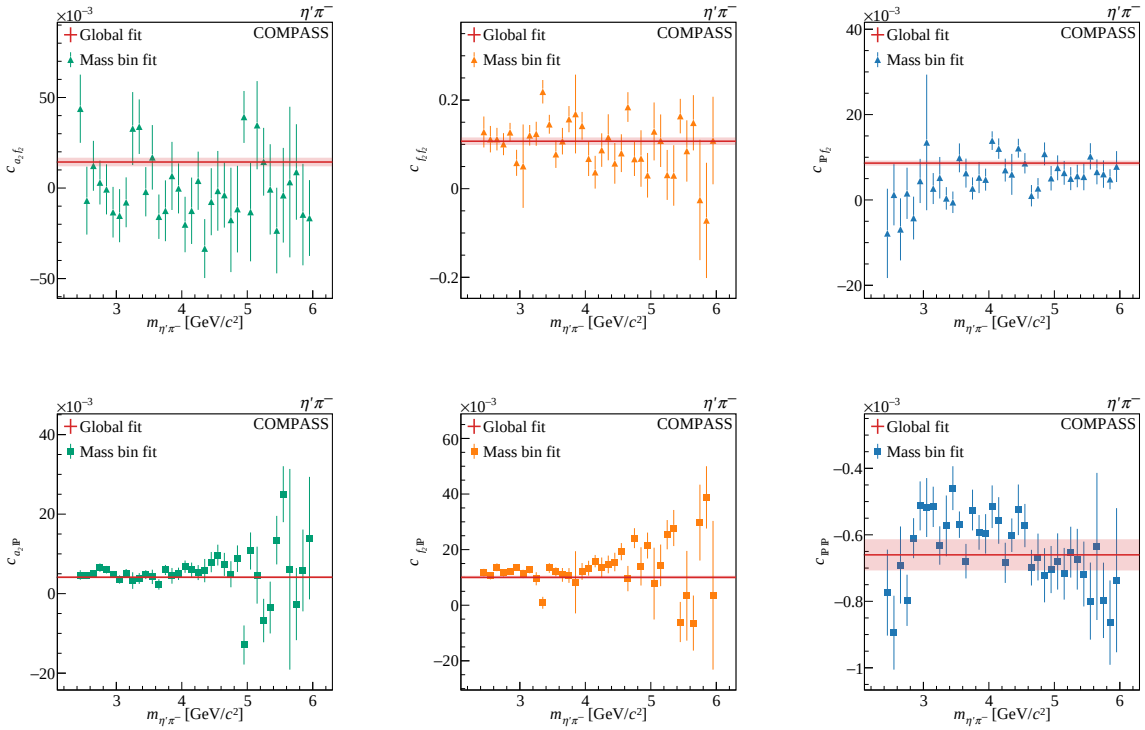


FIG. 11. $\eta'\pi^-$ strength parameters $\{c\}$ of the KGR + $a_2' + \pi_1$ fit for the leading ordinary exchanges. Conventions as in Fig. 9.

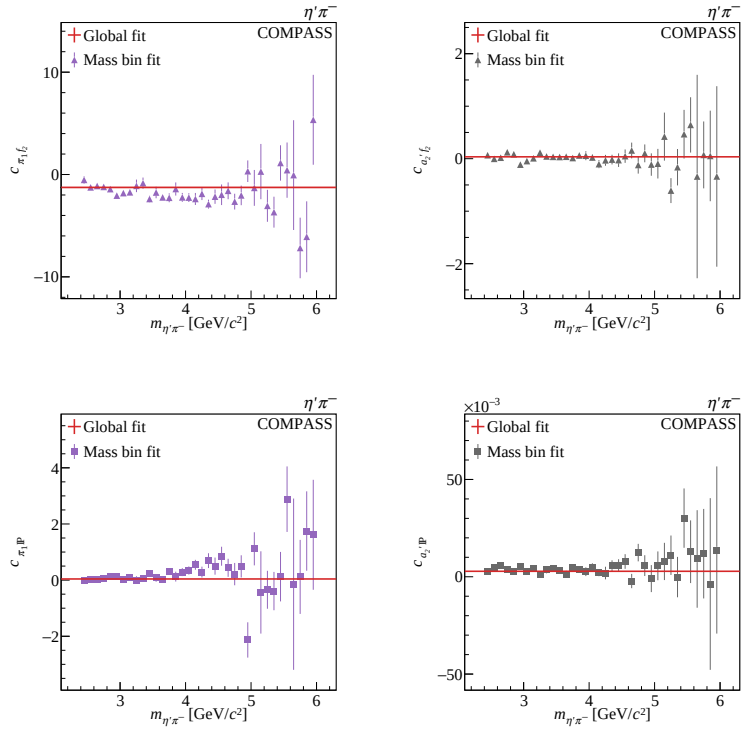


FIG. 12. $\eta'\pi^-$ strength parameters $\{c\}$ of the KGR $+ a_2' + \pi_1$ fit for the subleading $a_2'$ and exotic $\pi_1$ exchanges. Conventions as in Fig. 9.

## $\eta\pi^-$ DISTRIBUTIONS

In this section we compare the $\eta\pi^-$ weighted intensity distributions of the fits using the KGR (left), KGR $+ \pi_1 + a_2'$ (center-left), JPAC (center-right) and JPAC $+ \pi_1 + a_2'$ (right) models to the binned COMPASS data. The difference between KGR and JPAC fits provide an estimation of the systematic uncertainty associated to the leading ordinary exchanges. We present results depending on the invariant mass distribution $m_{\eta\pi}$ (Fig. 13), $t_\eta$ (Figs. 14 and 15), $t_\pi$ (Figs. 16 and 17), and $t_p$ (Figs. 18 and 19.) We provide the individual contributions of the exchanges as well as top $\pi_1$, top $a_2'$, top $a_2$, top $f_2$ and top $\mathbb{P}$ aggregates for $t_\eta$ and $t_\pi$ distributions (see Figs. 15 and 17), and bottom $f_2$ and bottom $\mathbb{P}$ aggregates for $t_p$ distribution (see Fig. 19.) Finally, we show the results for the forward-backward asymmetry in Fig. 20.

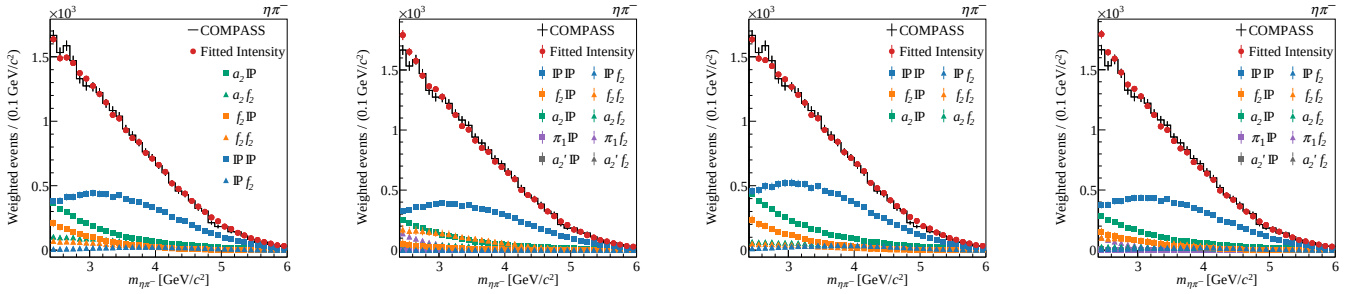


FIG. 13. $\eta\pi^-$ weighted intensity distributions dependence on $m_{\eta\pi}$. Left: KGR fit; Center-left: KGR $+ \pi_1 + a_2'$ fit; Center-right: JPAC fit; Right: JPAC $+ \pi_1 + a_2'$ fit. Binned COMPASS data is drawn in black. Diagrams with bottom $\mathbb{P}$ are marked with squares and those with bottom $f_2$ with triangles.

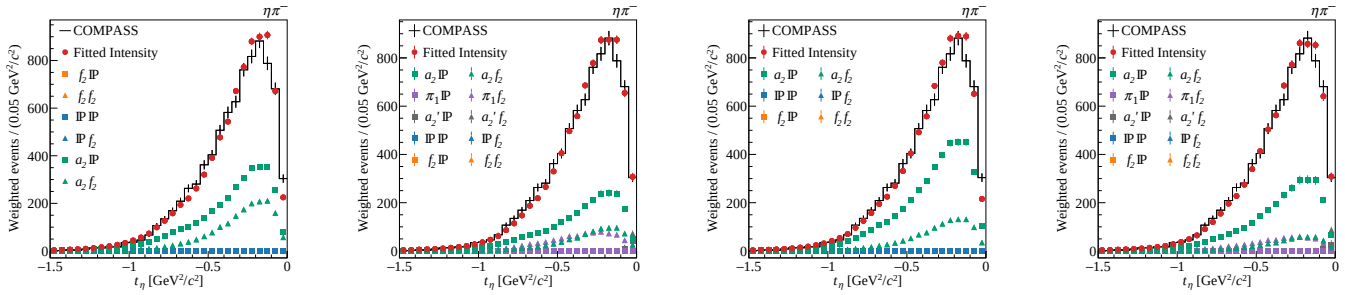


FIG. 14. $\eta\pi^-$ weighted intensity distributions dependence on $t_\eta$. Individual contributions. Left: KGR fit; Center-left: KGR $+ \pi_1 + a_2'$ fit; Center-right: JPAC fit; Right: JPAC $+ \pi_1 + a_2'$ fit. Conventions as in Fig. 13.

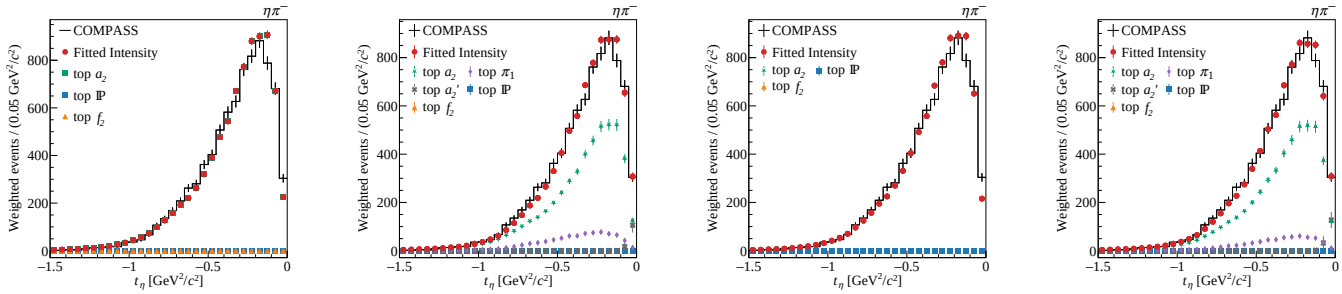


FIG. 15. $\eta\pi^-$ weighted intensity distributions dependence on $t_\eta$. Top Reggeon exchange contributions coherently summed. By top $\mathbb{P}$, top $f_2$, top $a_2$, top $a_2'$ and top $\pi_1$ we refer to the coherent sum of the amplitudes exchanged $\mathbb{R}_t$ is the $\mathbb{P}$, $f_2$, $a_2$, $a_2'$ and , $\pi_1$, respectively. Left: KGR fit; Center-left: KGR $+ \pi_1 + a_2'$ fit; Center-right: JPAC fit;Right: JPAC $+ \pi_1 + a_2'$ fit.

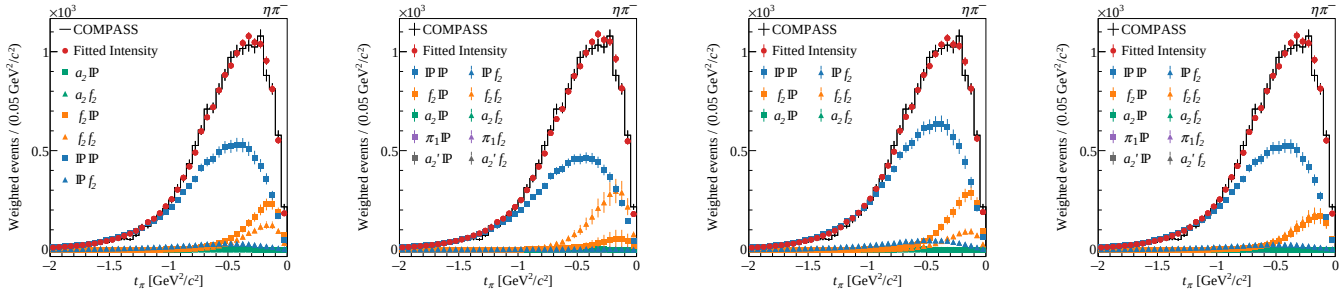


FIG. 16. $\eta\pi^-$ weighted intensity distributions dependence on $t_\pi$. Individual contributions. Left: KGR fit; Center-left: KGR $+ \pi_1 + a_2'$ fit; Center-right: JPAC fit; Right: JPAC $+ \pi_1 + a_2'$ fit. Conventions as in Fig. 13.

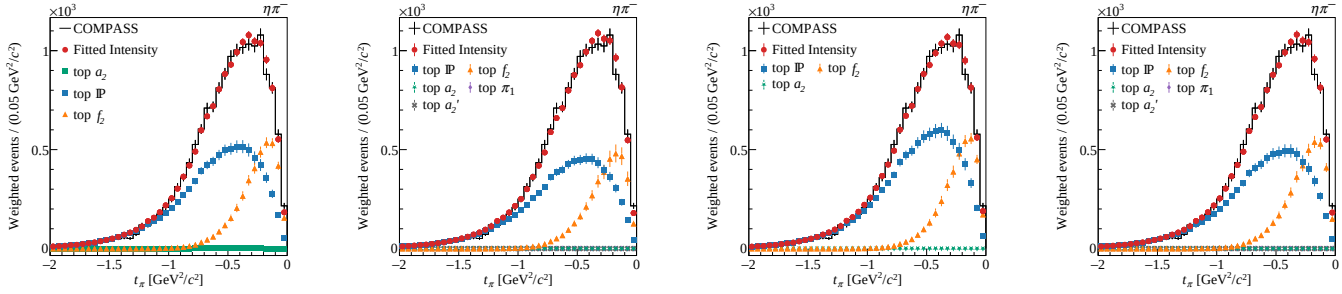


FIG. 17. $\eta\pi^-$ weighted intensity distributions dependence on $t_\pi$. Top Reggeon exchange contributions coherently summed. Left: KGR fit; Center-left: KGR $+ \pi_1 + a_2'$ fit; Center-right: JPAC fit; Right: JPAC $+ \pi_1 + a_2'$ fit. Conventions as in Fig. 15.

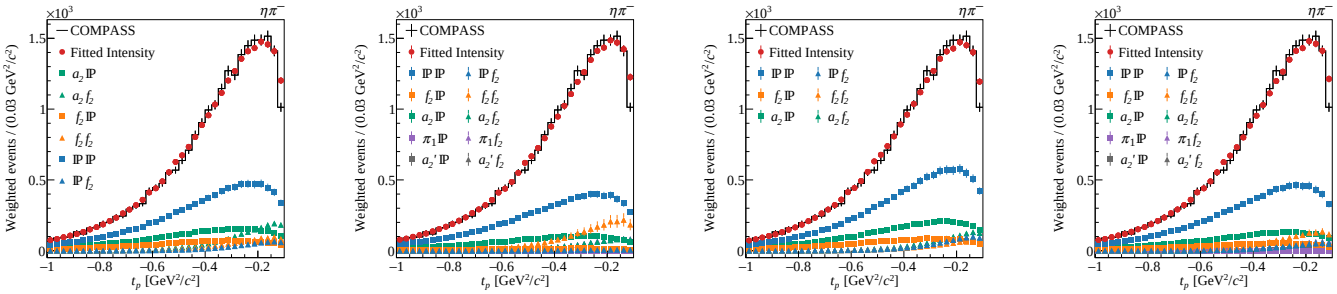


FIG. 18. $\eta\pi^-$ weighted intensity distributions dependence on $t_p$. Individual contributions. Left: KGR fit; Center-left: KGR + $\pi_1 + a_2'$ fit; Center-right: JPAC fit; Right: JPAC + $\pi_1 + a_2'$ fit. Conventions as in Fig. 13.

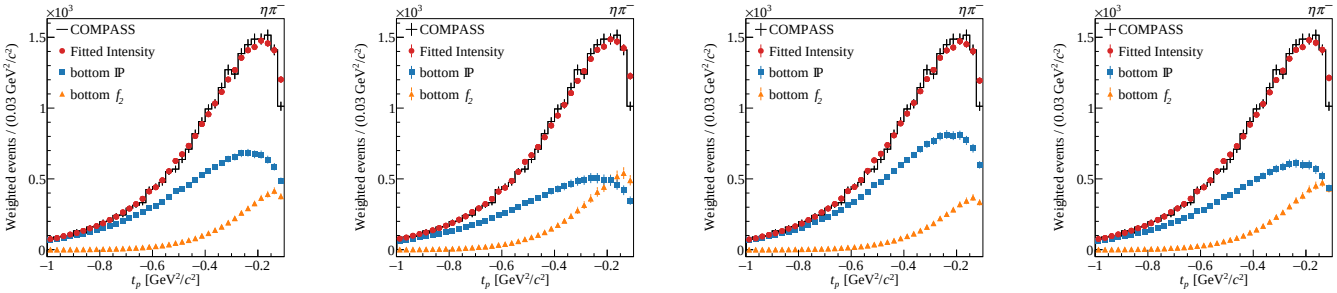


FIG. 19. $\eta\pi^-$ weighted intensity distributions dependence on $t_p$. Bottom Reggeon exchange contributions coherently summed. By bottom $\mathbb{P}$ (bottom $f_2$) we refer to the coherent sum of the amplitudes whose exchanged $\mathbb{R}_b$ is the $\mathbb{P}$ ($f_2$). Left: KGR fit; Center-left: KGR + $\pi_1 + a_2'$ fit; Center-right: JPAC fit; Right: JPAC + $\pi_1 + a_2'$ fit.

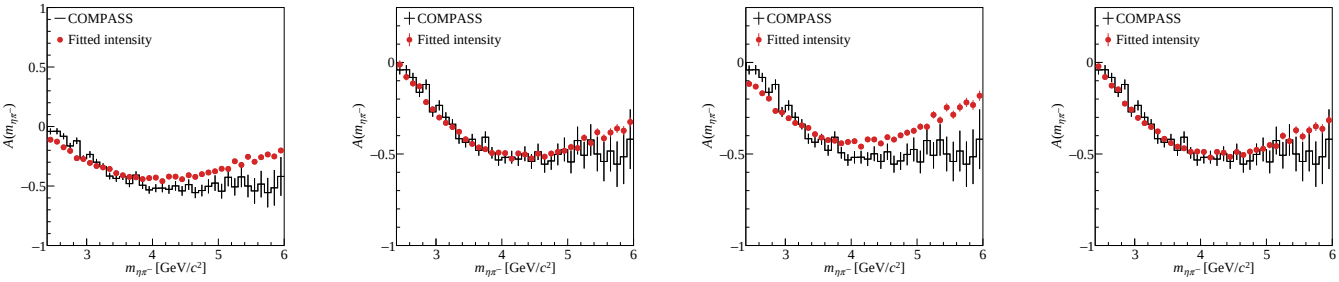


FIG. 20. $\eta\pi^-$ weighted forward-backward asymmetry distribution dependence on $m_{\eta\pi}$. Left: KGR fit; Center-left: KGR + $\pi_1 + a_2'$ fit; Center-right: JPAC fit; Right: JPAC + $\pi_1 + a_2'$ fit. Binned COMPASS data is drawn in black.

## $\eta'\pi^-$ DISTRIBUTIONS

In this section we compare the $\eta'\pi^-$ weighted intensity distributions of the fits using the KGR (left), KGR + $\pi_1 + a_2'$ (center-left), JPAC (center-right) and JPAC + $\pi_1 + a_2'$ (right) models to the binned COMPASS data. The difference between KGR and JPAC fits provide an estimation of the systematic uncertainty associated to the leading ordinary exchanges. We present results depending on the invariant mass distribution $m_{\eta'\pi}$ (Fig. 21), $t_{\eta'}$ (Figs. 22 and 23), $t_\pi$ (Figs. 24 and 25.) and $t_p$ (Figs. 26 and 27.) We provide the individual contributions of the exchanges as well as top $a_2$, top $f_2$, top $\mathbb{P}$, top $a_2'$ and top-$\pi_1$aggregates for $t_{\eta'}$ and $t_\pi$ distributions (see Figs. 23 and 25, and bottom $f_2$ and bottom $\mathbb{P}$ aggregates for $t_p$ distribution (see Fig. 27.) Finally, we show the results for the forward-backward asymmetry in Fig. 28.

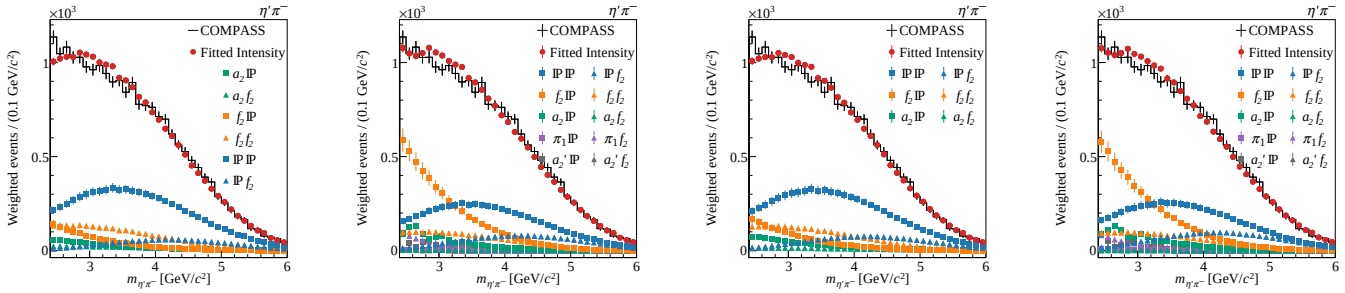


FIG. 21. $\eta'\pi^-$ weighted intensity distributions dependence on $m_{\eta\pi}$. Left: KGR fit; Center-left: KGR + $\pi_1 + a_2'$ fit; Center-right: JPAC fit; Right: JPAC + $\pi_1 + a_2'$ fit. Conventions as in Fig. 13.

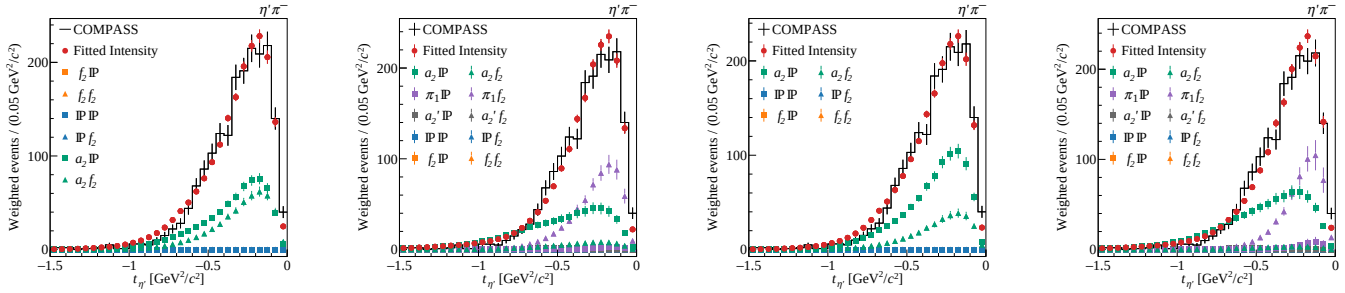


FIG. 22. $\eta'\pi^-$ weighted intensity distributions dependence on $t_\eta$. Individual contributions. Left: KGR fit; Center-left: KGR + $\pi_1 + a_2'$ fit; Center-right: JPAC fit; Right: JPAC + $\pi_1 + a_2'$ fit. Conventions as in Fig. 21.

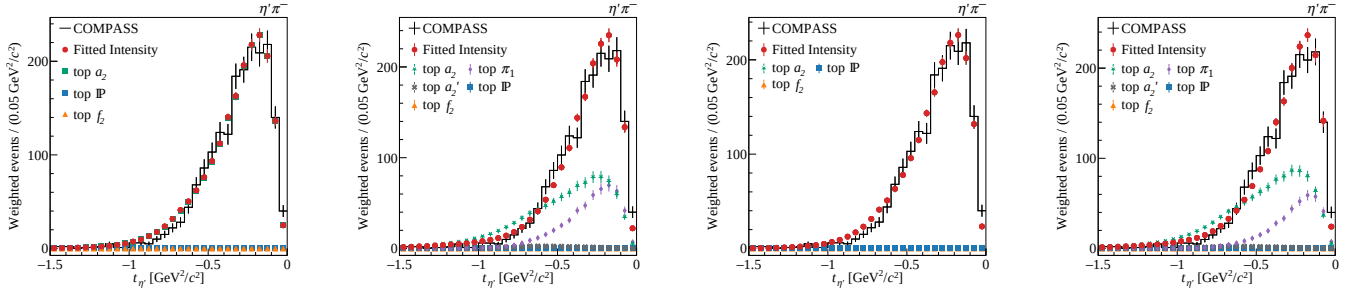


FIG. 23. $\eta'\pi^-$ weighted intensity distributions dependence on $t_\eta$. Top Reggeon exchange contributions coherently summed. Left: KGR fit; Center-left: KGR + $\pi_1 + a_2'$ fit; Center-right: JPAC fit; Right: JPAC + $\pi_1 + a_2'$ fit. Conventions as in Fig. 21.

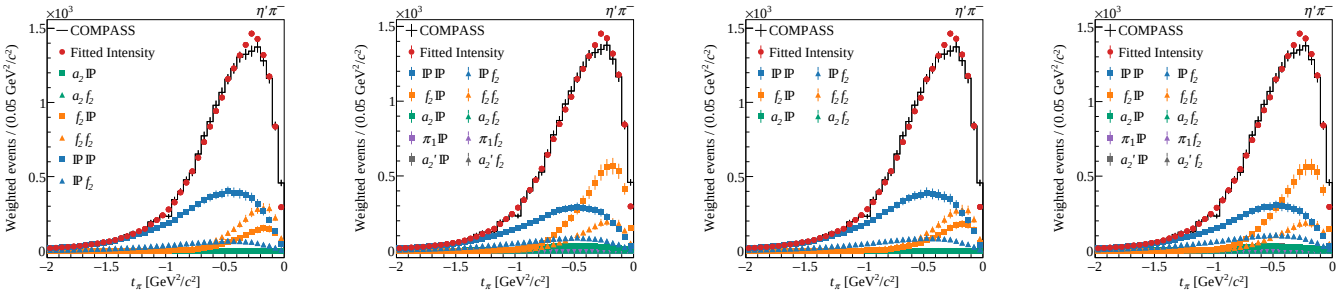


FIG. 24. $\eta'\pi^-$ weighted intensity distributions dependence on $t_\pi$. Individual contributions. Left: KGR fit; Center-left: KGR + $\pi_1 + a_2'$ fit; Center-right: JPAC fit; Right: JPAC + $\pi_1 + a_2'$ fit. Conventions as in Fig. 21.

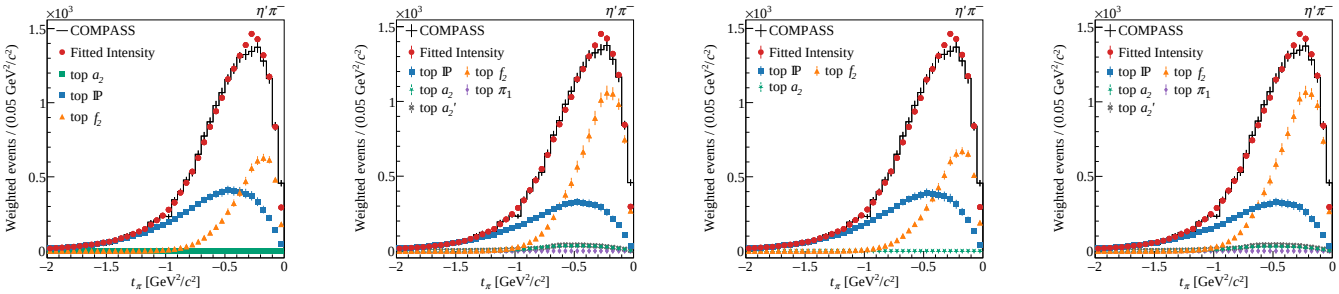


FIG. 25. $\eta'\pi^-$ weighted intensity distributions dependence on $t_\pi$. Top Reggeon exchange contributions coherently summed. Left: KGR fit; Center-left: KGR + $\pi_1 + a_2'$ fit; Center-right: JPAC fit; Right: JPAC + $\pi_1 + a_2'$ fit. Conventions as in Fig. 21.

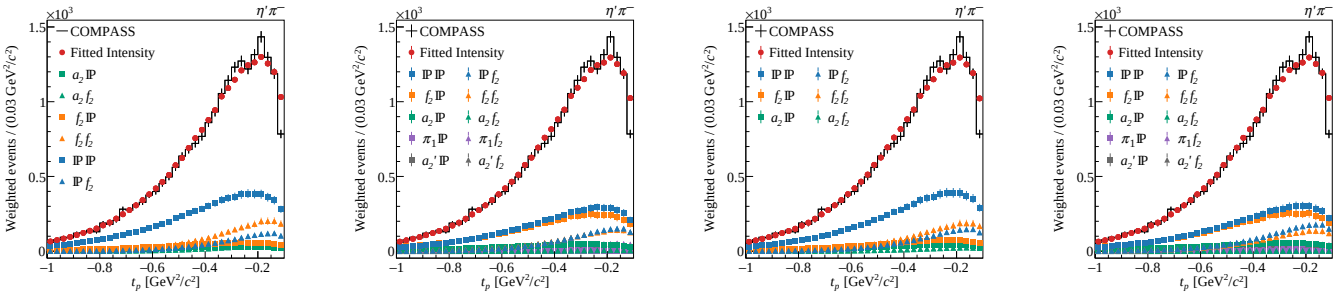


FIG. 26. $\eta'\pi^-$ weighted intensity distributions dependence on $t_p$. Individual contributions. Left: KGR fit; Center-left: KGR + $\pi_1 + a_2'$ fit; Center-right: JPAC fit; Right: JPAC + $\pi_1 + a_2'$ fit. Conventions as in Fig. 21.

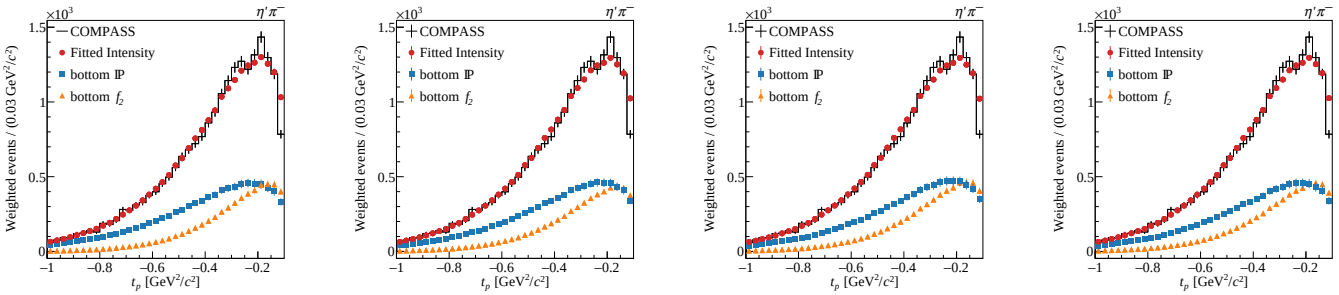


FIG. 27. $\eta'\pi^-$ weighted intensity distributions dependence on $t_p$. Bottom Reggeon exchange contributions coherently summed. Left: KGR fit; Center-left: KGR + $\pi_1 + a_2'$ fit; Center-right: JPAC fit; Right: JPAC + $\pi_1 + a_2'$ fit. Conventions as in Fig. 19.

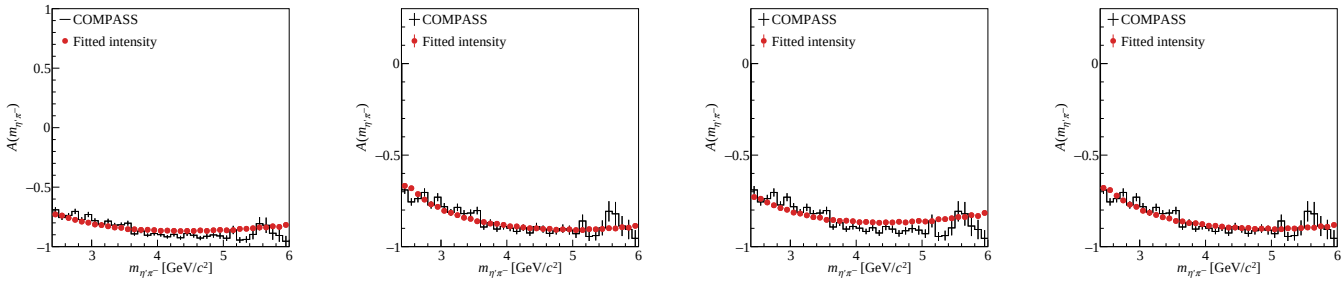


FIG. 28. $\eta'\pi^-$ weighted forward-backward asymmetry distribution dependence on $m_{\eta'\pi}$. Left: KGR fit; Center-left: KGR $+ \pi_1 + a_2'$ fit; Center-right: JPAC fit; Right: JPAC $+ \pi_1 + a_2'$ fit. Conventions as in Fig. 20.

## FITS IN THE $m_{\eta\pi} = [4, 6]\,\text{GeV}$ RANGE

For completeness, we show the results for the base model in the high invariant mass region $m_{\eta\pi} = [4, 6]\,\text{GeV}$ for both $\eta\pi^-$ and $\eta'\pi^-$ channels using the KGR Regge trajectories. Results are similar for the JPAC trajectories. Overall results are good in this energy range with some deviation in the description of the $\eta\pi^-$ asymmetry for the highest invariant masses, center-right plot in Fig. 29.

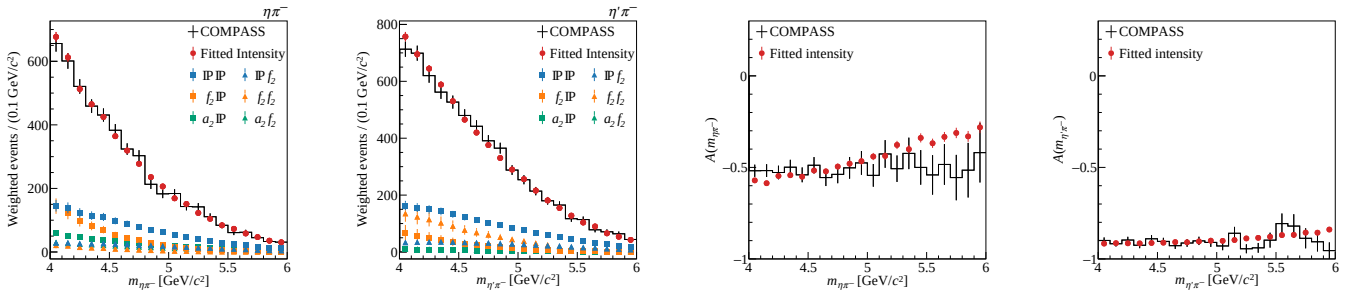


FIG. 29. Left ($\eta\pi^-$) and center left ($\eta'\pi^-$): Weighted intensity distributions dependence on $m_{\eta\pi}$. Center right ($\eta\pi^-$) and right ($\eta'\pi^-$): Weighted asymmetry distributions dependence on $m_{\eta\pi}$.

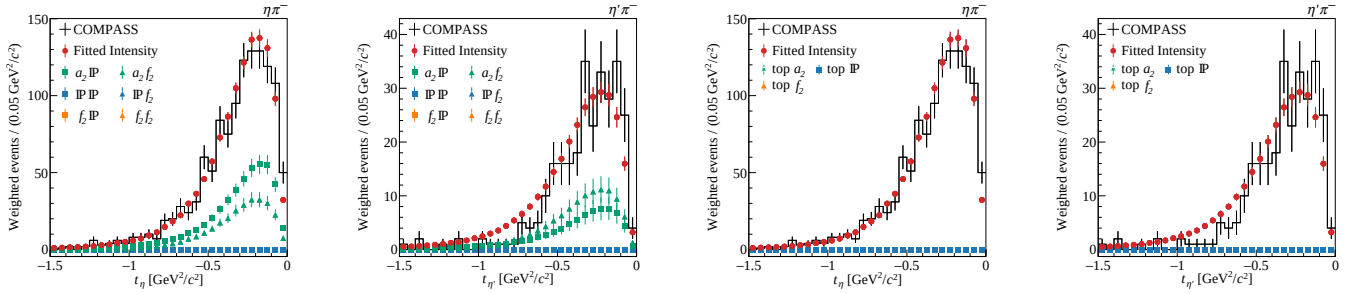


FIG. 30. Weighted intensity distributions dependence on $t_\eta$. Left ($\eta\pi^-$) and center left ($\eta'\pi^-$): individual contributions; center right ($\eta\pi^-$) and right ($\eta'\pi^-$): coherently summed top contributions.

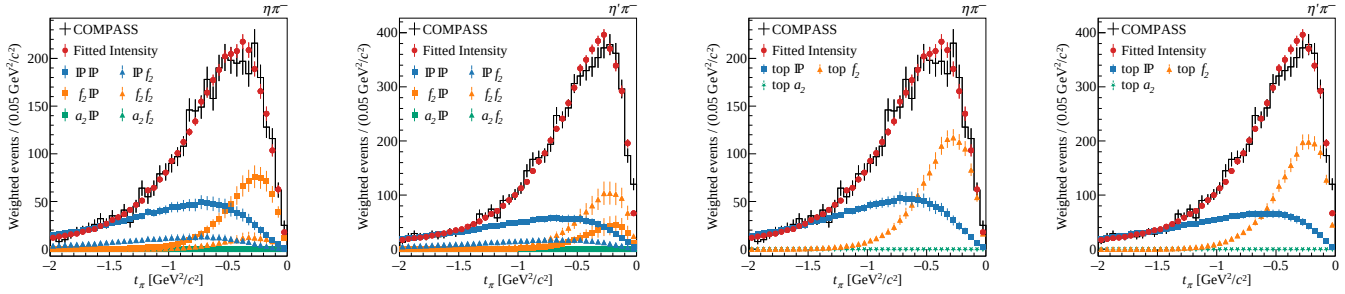


FIG. 31. Weighted intensity distributions dependence on $t_\pi$. Left ($\eta\pi^-$) and center left ($\eta'\pi^-$): individual contributions; center right ($\eta\pi^-$) and right ($\eta'\pi^-$): coherently summed top contributions.

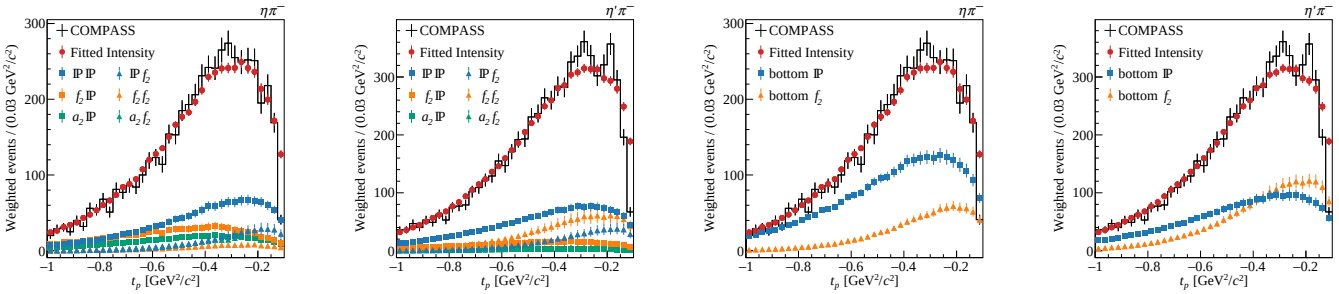


FIG. 32. Weighted intensity distributions dependence on $t_p$. Left ($\eta\pi^-$) and center left ($\eta'\pi^-$): individual contributions; center right ($\eta\pi^-$) and right ($\eta'\pi^-$): coherently summed top contributions.

## POMERON STUDIES

Finally, we study the impact of the Pomeron in the high energy behavior of the asymmetry. Results are shown in Fig. 33. First, on the left plot we show the impact of changing the Pomeron intercept of the top Pomeron exchange trajectory in the $\eta\pi^-$ asymmetry. This is an effective way to take into account corrections to the leading pole approximation which can be relevant for the $\eta^{(\prime)}\pi^-$ subsystem. We find that the agreement with the data can be improved, although the uncorrected Pomeron exchange already provides results within the experimental uncertainties. The center ($\eta\pi^-$) and right ($\eta'\pi^-$) plots show the theoretical forward-backward asymmetry for the KGR, KGR + $a_2'$ and KGR + $a_2'$ + $\pi_1$ fits, when it is not corrected by the detector effects. It is apparent that the asymmetry tends to $-1$ as expected from Pomeron dominance.

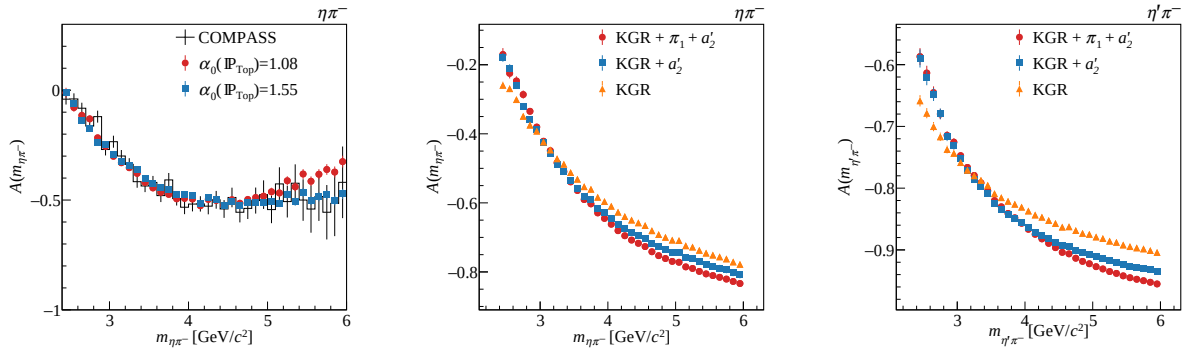


FIG. 33. Pomeron studies. Left: Impact of the variation of the Pomeron top exchange intercept. Center: Theory without acceptance corrections for the $\eta\pi^-$ forward-backward asymmetry. Right: Theory without acceptance corrections for the $\eta'\pi^-$ forward-backward asymmetry.